

# Optimal disturbances and large-scale energetic motions in turbulent boundary layers

Timothy B. Davis<sup>1,†</sup>, Ali Uzun<sup>1,‡</sup> and Farrukh S. Alvi<sup>1</sup>

<sup>1</sup>Department of Mechanical Engineering, FAMU-FSU College of Engineering, Florida Center for Advanced Aero-Propulsion (FCAAP), Florida State University, Tallahassee, FL 32310, USA

(Received 3 August 2017; revised 5 October 2018; accepted 8 October 2018;  
first published online 29 November 2018)

We examine disturbances leading to optimal energy growth in a spatially developing, zero-pressure-gradient turbulent boundary layer. The slow development of the turbulent mean flow in the streamwise direction is modelled through a parabolized formulation to enable a spatial marching procedure. In the present framework, conventional spatial optimal disturbances arise naturally as the homogeneous solution to the linearized equations subject to a turbulent forcing at particular wavenumber combinations. A wave-like decomposition for the disturbance is considered to incorporate both conventional stationary modes as well as propagating modes formed by non-zero frequency/streamwise wavenumber and representative of convective structures naturally observed in wall turbulence. The optimal streamwise wavenumber, which varies with the spatial development of the turbulent mean flow, is computed locally via an auxiliary optimization constraint. The present approach can then be considered, in part, as an extension of the resolvent-based analyses for slowly developing flows. Optimization results reveal highly amplified disturbances for both stationary and propagating modes. Stationary modes identify peak amplification of structures residing near the centre of the logarithmic layer of the turbulent mean flow. Inner-scaled disturbances reminiscent of near wall streaks, and amplified over short streamwise distances, are identified in the computed streamwise energy spectra. In all cases, however, propagating modes surpass their stationary counterpart in both energy amplification and relative contribution to total fluctuation energy. We identify two classes of large-scale energetic modes associated with the logarithmic and wake layers of the turbulent mean flow. The outer-scaled wake modes agree well with the large-scale motions that populate the wake layer. For high Reynolds numbers, the log modes increasingly dominate the energy spectra with the predicted streamwise and wall-normal scales in agreement with superstructures observed in turbulent boundary layers.

**Key words:** boundary layers, boundary layer stability, turbulent boundary layers

---

† Email address for correspondence: [tbdavis@fsu.edu](mailto:tbdavis@fsu.edu)

‡ Present address: National Institute of Aerospace, 100 Exploration Way, Hampton, VA 23666, USA

## 1. Introduction

The existence of organized, coherent motions is now recognized as a robust feature of wall-bounded turbulence, persisting over a wide range of Reynolds numbers and in a variety of canonical flow configurations. A number of studies over the past several decades have focused on the identification and description of such motions (Robinson 1991), highlighting their roles in turbulence production and self-sustainment (Panton 2001) and their contributions to turbulent kinetic energy and Reynolds stress (Balakumar & Adrian 2007). Recent studies report that, especially with regard to the largest scales, their effects become increasingly important with increasing Reynolds number (Hutchins & Marusic 2007a; Smits, McKeon & Marusic 2011). Apart from a level of fundamental understanding, the persistent and surprisingly regular patterns seem to imply that, despite all its complexity, at least some features of wall turbulence may be well described by low-dimensional models (Sharma & McKeon 2013). To this end, significant progress has been made in describing these ‘structures’ using simple, linear analyses which leverage the amplification properties of the Navier–Stokes equations (e.g. McKeon & Sharma 2010). In this study, we extend these approaches to the non-parallel turbulent boundary layer, in which the spatial development of the mean flow plays a role in the preferential selection of the large-scale motions. Ultimately, a description of such motions, including their relation and interaction with mean flow, is a crucial step in understanding, and potentially controlling, wall turbulence. In what follows, we briefly review the energetic structures observed in canonical wall-bounded turbulent flows, particularly the turbulent boundary layer, and highlight recent theoretical approaches to predicting these based on predominantly linear analysis tools.

### 1.1. Organized motions in wall turbulence

There are, at least currently, four types of organized motions generally recognized in wall-bounded turbulent flows: near wall streaks, hairpin vortices, large-scale motions (LSMs) and very large-scale motions (VLSMs) or superstructures in boundary layers (Smits *et al.* 2011). Of these, hairpin vortices, or inclined horseshoe-shaped vortical structures with heads aligned with the mean shear, were first identified by Theodorsen (1952). Numerous studies (e.g. see Head & Bandyopadhyay 1981, Robinson 1991, Adrian 2007, Wu & Moin 2009) have since confirmed the existence of hairpin vortices and hairpin packets in wall-bounded turbulent flows; however, their relevance and existence in fully developed, high Reynolds number turbulence remains controversial (see, for example, Eitel-Amor *et al.* 2015). The remaining coherent motions, namely the near wall streaks, LSMs and VLSMs can be loosely categorized as ‘streaky’ structures, with their streamwise scales generally much larger than their spanwise and wall normal scales. The most widely studied of which are the near wall, quasi-periodic streamwise vortices and velocity streaks originally visualized by Kline *et al.* (1967) and associated with the inner peak in streamwise energy spectra. These ubiquitous structures appear to be part of a near wall autonomous cycle (Jiménez & Pinelli 1999) and populate the buffer region of the mean velocity profile, centred at approximately 15 viscous units from the wall with average spanwise spacing and streamwise lengths of 100 and 1000 viscous units, respectively. Of particular importance is the role of the near wall streaks in turbulence production and self-sustainment.

More recent studies on higher Reynolds number flows, coupled with the advancement of experimental techniques and computational power, have identified the LSMs and VLSMs. The LSMs are recognized as structures with a streamwise scale of

approximately 2–3 outer units (i.e. channel half-height  $h$ , pipe radius  $R$  or boundary layer height  $\delta$ ) and are suggested to be formed by the streamwise alignment of hairpin vortex packets which in turn induce elongated regions of low momentum fluid between their legs (Adrian, Meinhart & Tomkins 2000; Tomkins & Adrian 2003; Hutchins, Hambleton & Marusic 2005; Dennis & Nickels 2011a). Their spanwise scales appear to scale with outer units, with typical sizes of approximately  $0.5\text{--}1\delta$  (Tomkins & Adrian 2005).

Very long regions of low momentum fluid, often paired in the spanwise direction with regions of high momentum fluid, form the VLMSs in pipes and channels and superstructures in boundary layers (Kim & Adrian 1999; Hutchins & Marusic 2007a; Dennis & Nickels 2011b). The streamwise scale of the VLMSs are often an order of magnitude above the outer length scale, with instantaneous structures identified using visualization techniques extending up to  $15\text{--}30R$  in pipes and channels and  $10\text{--}20\delta$  in boundary layers. These motions are associated with the outer peak in the streamwise energy spectra ( $\sim 6\delta$  or  $\sim 10\text{--}20R$ ) that emerges at higher Reynolds number with sufficient scale separation (Hutchins & Marusic 2007b; Marusic, Mathis & Hutchins 2010). Hutchins & Marusic (2007a) noted that the regions of low/high momentum tend to meander in the spanwise direction as they convect downstream, causing the often reported single point measurements of the streamwise energy spectra to potentially underestimate the true length of the structures. Further, the same authors showed the LSMs and VLMSs affect the near wall events by means of an amplitude modulation, meaning the streamwise energy spectra cannot have a purely inner-scaled region. Several studies have since verified these long wavelength motions are indeed active in that they carry a significant fraction ( $\sim 50\%$ ) of turbulent kinetic energy and Reynolds stress (e.g. Balakumar & Adrian 2007).

Although qualitatively similar, the VLMSs in pipes and channels and the superstructures in boundary layers have apparent quantitative differences, as highlighted by Monty *et al.* (2009). On average, the length of the most energetic large structures appear approximately fixed in outer units for each canonical flow. As previously noted, however, internal flows support much longer structures than external flows, with the streamwise energy spectra in boundary layers identifying energetically dominant outer structures at  $\lambda_x \approx 6\delta$  as opposed to the  $10 < \lambda_x/R < 20$  in internal flows. Here,  $x$  denotes the streamwise coordinate and  $\lambda$  the wavelength. Unlike pipes and channels, where the VLMSs maintain appreciable energy content into the wake region of the turbulent mean flow, the superstructures in boundary layers appear confined to the logarithmic region. Outside, a rapid shortening of streamwise scales occurs such that the wake is dominated by LSMs with  $\lambda_x \approx 3\delta$  (Monty *et al.* 2009). Mathis, Hutchins & Marusic (2009) and Marusic *et al.* (2010) showed that the wall-normal location of the outer peak in the streamwise energy spectra scaled well with the geometric mean of the logarithmic overlap layer for increasing Reynolds number. This requires the wall-normal location scaled in viscous units to increase with the square root of the friction Reynolds number,  $Re_\tau = \delta u_\tau/\nu$ , where  $u_\tau$  is the wall friction velocity and  $\nu$  the kinematic viscosity. Similarly, the peak location in outer units, scaled by boundary layer thickness, decreases as  $Re_\tau^{-1/2}$ .

Of particular relevance to the present study, the spanwise scaling of superstructures with increasing Reynolds number has received considerably less attention. Streamwise scales can, at least approximately, be deduced experimentally from time-resolved single point measurement coupled with Taylor's hypothesis, or directly from simulations in large streamwise domains. Estimations of spanwise scales, however, are more difficult requiring multi-point measurements distributed across the span or

global field measurements with large spanwise domain. This is burdensome both experimentally and computationally for large Reynolds numbers. Recent studies seem to indicate the spanwise scales of superstructures may scale with outer units such as  $\delta$ , (Eitel-Amor, Örlü & Schlatter 2014) with  $\lambda_z \sim O(\delta)$ , but higher Reynolds number studies are needed.

### 1.2. A review of gain-based approaches to the formation of energetic motions

The fact that such energetic, organized motions have been repeatedly observed supports conceptually a strong amplification mechanism present in the Navier–Stokes equations, even in fully developed turbulent flows. Several recent studies have focused on linear dynamics, highlighting the importance of linear transient amplification mechanisms in turbulent flows. Absent an inflectional instability present in free shear, canonical wall-bounded turbulent flows are shown to be stable to modal solutions of the linearized disturbance equations (i.e. all eigenvalues of the linearized operator lie in the stable half-plane (Reynolds & Tiederman 1967)). As in laminar shear flows, however, turbulent shear flows are susceptible to potentially large transient energy amplification, as evident in the Orr–Sommerfeld and Squire equations, when the wall-normal vorticity is forced by the wall-normal velocity through the spanwise modulation of the mean shear (Ellingsen & Palm 1975; Landahl 1980; Schmid & Henningson 2001). The importance of this linear coupling term in the production and sustainment of wall-bounded turbulence was emphasized in the direct numerical simulation of Kim & Lim (2000).

The potential for transient growth of disturbance energy is related to the non-normality of the Navier–Stokes equations. When linearized about an equilibrium solution, the resulting linear operator exhibits strong non-normality in the presence of high shear in the base state. In this case, the superposition of non-orthogonal eigenmodes can lead to short-term energy growth of several orders of magnitude, even in the absence of an unstable eigenvalue. This concept was first leveraged in a variety of laminar shear flows to explain transition in flows that are either stable to exponentially growing disturbances, or are found to transition at conditions much earlier than that predicted by modal analysis. By optimizing kinetic energy over all initial conditions, the disturbance which achieved maximum energy amplification at a prescribed time was shown to amplify up to several thousand times the initial value (Gustavsson 1991; Butler & Farrell 1992; Reddy & Henningson 1993). In all cases, the so-called optimal disturbances correspond to initial spanwise periodic, streamwise vortices that induce streamwise velocity streaks, infinitely elongated in the streamwise direction. The optimization is typically extended over all spanwise wavenumbers, and for all time, to determine the global optimum in energy amplification. Of primary relevance to the present work, the initial parallel, temporal analyses were extended by Andersson, Berggren & Henningson (1999) and Luchini (2000) using an iterative adjoint-based procedure to consider the spatial growth of streamwise elongated disturbances in a non-parallel Blasius boundary layer. The motivation is to describe the streaky structures that develop in laminar boundary layer subject to high free-stream turbulence levels and cause rapid transition to turbulence (Matsubara & Alfredsson 2001). While qualitatively similar to the results of Butler & Farrell (1992), it was shown that the spatial framework, which accounted for the streamwise development of the base flow, resulted in optimal spanwise wavelengths approximately 20% smaller ( $\sim 3\delta$ ) than the parallel, temporal analysis. As discussed by both Andersson *et al.* (1999) and Luchini (2000), the linearized equations are highly selective in that the

optimal disturbance (leading singular value) is well separated from other sub-optimal modes. The consequence is that, so long as a given input has a non-negligible component in the direction of the optimal disturbance, the corresponding response will be principally in the direction of the optimal output disturbance. In other words, a random velocity disturbance can be expected to develop into a streamwise velocity streak.

The physical reasoning by which disturbances transiently amplify and develop into streamwise elongated streaky structures of low/high momentum is often attributed to the lift-up effect (Ellingsen & Palm 1975; Landahl 1980). In this inviscid model, transverse velocities locally displace a fluid element and, in the presence of shear, produce a velocity disturbance which may grow as fast as linear in time. This argument was originally put forth by Landahl (1980) as a possible mechanism for the formation of near wall streaks in turbulent boundary layers. As such, the optimal disturbances well studied in laminar shear flows have recently been adopted to describe the formation of streaky structures about turbulent mean flows. Butler & Farrell (1993) considered the formation of near wall streaks in turbulent channel flow and found good agreement between the predicted spanwise scales of the optimal disturbances by constraining the optimization times to typical eddy turnover times. Linearizing about a turbulent mean flow, however, introduces unknown Reynolds stresses into the governing equations. Using the approach of Reynolds & Hussain (1972), del Álamo & Jiménez (2006) extended the analysis of Butler & Farrell (1993) by modelling the unknown Reynolds stresses through an isotropic eddy viscosity determined from the mean flow. Without any *a priori* constraint on the optimization time, del Álamo & Jiménez (2006) identified two peak spanwise wavelengths, one that scaled in outer units with  $\lambda_z \approx 3h$  and a second that scaled with viscous units with  $\lambda_z^+ \approx 100$ . Cossu, Pujals & Depardon (2009) followed the same approach for a turbulent boundary layer, assuming a locally parallel flow approximation. Similar to the channel flow analysis of del Álamo & Jiménez (2006), Cossu *et al.* (2009) identified two peak spanwise wavelengths with an inner and outer scaling. The inner-scaled peak, with  $\lambda_z^+ \approx 82$ , agrees well with the previous analyses and experimental values for the characteristic spacing of the near wall structures. The outer peak, however, was found to occur for very large structures with spanwise wavelengths  $\lambda_z \approx 8\delta$ . Aside from the optimal disturbance approach, which characterizes the system response to initial conditions, several recent studies have also considered the response to external harmonic and stochastic forcing with similar results in terms of spanwise scale as optimal disturbances (e.g. Hwang & Cossu 2010).

More recently, McKeon & Sharma (2010) have addressed the ambiguity associated with the optimal disturbance formulation with a resolvent-based analysis and critical layer argument to identify the most energetically dominant structures in turbulent pipe flow. In practice, coherent structures observed in turbulent boundary layers are known to convect downstream with a speed at least approximately equal to the local mean flow. However, in the classical optimal disturbance formulation, the most amplified solutions are generally associated with zero streamwise wavenumber (Cossu *et al.* 2009), or zero frequency (Luchini 2000) such that they are infinitely elongated, stationary disturbances. We note that Hack & Moin (2017) have also recently examined propagating modes in the spatially developing Blasius boundary layer. Alternatively, McKeon & Sharma (2010) examined travelling wave solutions, formed by finite streamwise wavenumber–frequency pairs limited to physically observed scales, showing large amplification when the phase velocity of the disturbance approaches the local mean velocity. The resolvent formulation performs no explicit



linearization; the nonlinear terms are lumped into an unknown internal forcing that act in a feedback loop to the linear terms. Only the turbulent mean flow is assumed known and essentially acts as a filter to the class of possible scales. However, the resulting linear operator is identical to equations linearized about the turbulent mean flow in Reynolds & Hussain (1972) and subsequent analyses following the same approach (after neglecting the Reynolds stress term, typically referred to as a quasi-laminar analysis). McKeon & Sharma (2010) viewed this linear sub-system as a highly directional amplifier and showed that the resolvent formulation was able to identify structures consistent with scaling observed in turbulent pipe flows, in particular the VLSMs. Using the same decomposition, Sharma & McKeon (2013) showed that relatively few resolvent modes could be superposed to create structures resembling complex hairpin packets in turbulent boundary layers, highlighting the low-dimensional nature of the coherent structures in wall turbulence. Moarref *et al.* (2013) extended the analysis to turbulent channel flow, focusing on the scaling of the streamwise energy spectra. The authors identified three classes of travelling wave solutions associated with the inner, outer and logarithmic overlap regions of the mean flow. Favourable agreement was found between the energetically dominant scales observed in turbulent channel flow, again with the best agreement for the VLSMs where the peak wall-normal contribution scaled well with the geometric mean of the logarithmic region as observed experimentally.

### 1.3. Objectives of the current study and paper outline

In all previous gain-based studies focusing on wall-bounded turbulence, the mean flow has either been parallel or the parallel flow approximation has been made. Consequently, the disturbances have been assumed to develop locally rather than under a spatially developing mean flow. The slow change in boundary layer thickness, or equivalently local Reynolds number, is commonly invoked as argument for the parallel flow approximation. This, however, neglects both the lifetime of these structures and any history effect that may be present in the preferential selection of scales by the mean flow.

For the largest scales of interest, empirically say  $O(20\delta)$  in the streamwise direction, the change in boundary layer thickness is appreciable ( $\sim 40\%$ ). On average, these structures are likely formed far upstream of where they are observed, where the mean flow is invariably different. In temporal optimal disturbances, Cossu *et al.* (2009) reported optimization times of several hundred convective units based on the local boundary layer thickness for the most amplified disturbances. Over the equivalent streamwise extent, the boundary layer thickness would more than double during the disturbance lifetime. As such, we may expect significant quantitative differences in the selection of scales, in particular the large-scale structures, when the spatial growth of the turbulent boundary layer is considered.

In the present study, we formulate the optimal disturbance problem in a spatial framework, similar to that of Andersson *et al.* (1999) and Luchini (2000). An important distinction is made, however, which also allows the analysis of energetically dominant traveling waves within the spatial optimal disturbance framework. Although not specifically addressed in the present study, we also highlight the role of the unknown forcing term, similar to McKeon & Sharma (2010), Beneddine *et al.* (2016), to unify the connection between the present optimal disturbance framework and resolvent analysis.

In what follows, we review the governing equations, linearized model and establish the connection with structures observed in real turbulent flows in § 2. Here the

problem is formulated to determine the disturbances which optimally amplify over a given streamwise extent and the numerical implementation is outlined. In §3, conventional optimal disturbance results are presented corresponding to steady, infinitely elongated structures (in terms of streamwise wavelength, as the growth of the disturbances are ‘transient’ in space). In §4, these results are extended to travelling wave disturbances, where focus is given to scales which contribute dominantly towards total fluctuation energy. In contrast to previous optimal disturbance approaches, these propagating modes surpass their steady counterpart in both overall amplification and relative energy content. We also examine the scaling of the optimal streamwise and spanwise scales with increasing Reynolds number. A summary and discussion of the relevant findings of the present work is provided in §5.

## 2. Model formulation

In this section, we develop a model to explore the amplification properties of the Navier–Stokes equations in which the mean flow is allowed to vary slowly in the streamwise direction. The goal is to examine a harmonic decomposition of the governing equations which permits the study of both non-modal and critical layer behaviour while retaining the underlying inhomogeneities in a computationally accessible manner. The derivation follows closely the classical parabolized stability equations (PSE) and spatial optimal disturbances, slightly modified to extract the most energetic motions about a turbulent mean.

We begin with the incompressible Navier–Stokes equations,

$$\frac{\partial \mathbf{u}}{\partial t} + \mathbf{u} \cdot \nabla \mathbf{u} = -\nabla p + \nu \nabla^2 \mathbf{u}, \quad (2.1)$$

with the continuity constraint  $\nabla \cdot \mathbf{u} = 0$ , where  $\mathbf{u}$ ,  $p$  and  $\nu$  represent the fluid velocity, modified pressure and kinematic viscosity, respectively. We consider the fluctuating velocity and pressure field about a long time-averaged mean flow such that the instantaneous state is given by the Reynolds decomposition  $(\mathbf{u}, p) = \mathbf{q} = \bar{\mathbf{q}} + \mathbf{q}'$ . Here, the overbar and prime are used to denote the mean and fluctuating quantities, respectively. Substitution of the Reynolds decomposition into (2.1), it can be shown the mean flow field satisfies

$$\bar{\mathbf{u}} \cdot \nabla \bar{\mathbf{u}} + \overline{\mathbf{u}' \cdot \nabla \mathbf{u}'} = -\nabla \bar{p} + \nu \nabla^2 \bar{\mathbf{u}}, \quad (2.2)$$

with the fluctuations governed by

$$\frac{\partial \mathbf{u}'}{\partial t} + \bar{\mathbf{u}} \cdot \nabla \mathbf{u}' + \mathbf{u}' \cdot \nabla \bar{\mathbf{u}} = -\nabla p' + \nu \nabla^2 \mathbf{u}' - \mathbf{u}' \cdot \nabla \mathbf{u}' + \overline{\mathbf{u}' \cdot \nabla \mathbf{u}'}, \quad (2.3)$$

where both the mean and fluctuating quantities satisfy continuity,  $\nabla \cdot \bar{\mathbf{u}} = 0$  and  $\nabla \cdot \mathbf{u}' = 0$ . Clearly, (2.2) and (2.3) are coupled through the Reynolds stresses  $-\overline{\mathbf{u}' \cdot \nabla \mathbf{u}'}$ . However, if the mean flow is known *a priori*, either from experiment, computation or modelling, the closure problem in (2.3) is avoided. Following McKeon & Sharma (2010), Beneddine *et al.* (2016), we define  $\mathbf{f}' = \overline{\mathbf{u}' \cdot \nabla \mathbf{u}'} - \mathbf{u}' \cdot \nabla \mathbf{u}'$  as a turbulent forcing term encapsulating the nonlinearity in (2.3). Note that, in the present study, we do not explicitly consider the treatment of the nonlinear term,  $\mathbf{f}'$ , such that the resulting analysis can be seen as a linearized analysis of the Navier–Stokes equations about the turbulent mean. However,  $\mathbf{f}'$  is carried through the following discussion to draw comparisons with previous studies.

2.1. Harmonic decomposition for non-parallel boundary layers

We consider a turbulent boundary layer developing on a flat plate with constant free-stream velocity. The mean flow is assumed homogeneous along the span, but develops slowly in the streamwise direction and varies rapidly in the wall-normal direction. As such, the fluctuations  $\mathbf{q}'$  in (2.3) may be Fourier transformed in the homogeneous spanwise direction and in time. Unless a locally parallel flow approximation is made, however, the streamwise development of  $\bar{\mathbf{u}}$  precludes a decomposition of  $\mathbf{q}'$  into Fourier modes with constant streamwise wavenumber. Following a PSE-like decomposition, a spatially evolving field of constant frequency  $\omega$  and spanwise wavenumber  $\beta$  may be described by

$$\mathbf{q}'(\mathbf{x}, t) = \hat{\mathbf{q}}(x, y) \exp[i\Theta(x, z, t)], \tag{2.4}$$

$$\Theta(x, z, t) = \int_{x_0}^x \alpha(\xi) d\xi + \beta z - \omega t, \tag{2.5}$$

where the streamwise wavenumber is represented by  $\alpha = \alpha(x)$  and the spatial coordinates by  $x, y, z$  for the streamwise, wall-normal and spanwise directions, respectively. Equation (2.4) then decomposes the fluctuating field into a wave-like component described by the exponential term with corresponding amplitudes  $\hat{\mathbf{q}}$ . These functions or ‘modes’ are convective, or form travelling waves, with local phase speed  $c = \omega/\alpha$ . Note that because the decomposition (2.4) is the product of two  $x$ -dependent functions, an ambiguity arises as both oscillations and energy growth/decay may be absorbed into either the amplitude functions  $\hat{\mathbf{q}}$  or the exponential term for  $\alpha \in \mathbb{C}$ . In this study, we take  $\alpha$  to be a strictly real parameter such that streamwise oscillations are contained in the exponential and absorb the fluctuation energy into the amplitude functions. An auxiliary constraint is then implemented to determine the streamwise variation of  $\alpha$ . A similar approach has been considered in Tempelmann, Hanifi & Henningson (2010) to capture non-modal growth in three-dimensional laminar boundary layers, although the specification of the real streamwise wavenumber was done differently. Details of the method for determining  $\alpha(x)$ , and a comparison with the classical PSE approach, are delayed until § 2.5. The same decomposition may then be considered for the turbulent forcing term, such that  $\mathbf{f}' = \hat{\mathbf{f}}(x, y) \exp[i\Theta(x, z, t)]$ .

Substitution of (2.4) into (2.3) yields an equation governing the global spatial distribution of the amplitude functions  $\hat{\mathbf{q}}(x, y)$ . However, as the boundary layer develops slowly in the streamwise direction, this implies both the amplitude functions and streamwise wavenumber  $\alpha$  are also slowly varying in  $x$ . Formally, we may introduce a conventional boundary layer scaling to eliminate terms  $O(Re^{-2})$  and higher to obtain

$$\frac{\partial \hat{u}}{\partial x} + i\alpha \hat{u} + \frac{\partial \hat{v}}{\partial y} + i\beta \hat{w} = 0, \tag{2.6}$$

$$\begin{aligned} -i\omega \hat{u} + \bar{u} \left( \frac{\partial \hat{u}}{\partial x} + i\alpha \hat{u} \right) + \bar{v} \frac{\partial \hat{u}}{\partial y} + \hat{u} \frac{\partial \bar{u}}{\partial x} + \hat{v} \frac{\partial \bar{u}}{\partial y} \\ = -\frac{\partial \hat{p}}{\partial x} - i\alpha \hat{p} + \frac{1}{Re} \left( \frac{\partial^2 \hat{u}}{\partial y^2} - (\alpha^2 + \beta^2) \hat{u} \right) + \hat{f}_u, \end{aligned} \tag{2.7}$$

$$\begin{aligned} -i\omega \hat{v} + \bar{u} \left( \frac{\partial \hat{v}}{\partial x} + i\alpha \hat{v} \right) + \bar{v} \frac{\partial \hat{v}}{\partial y} + \hat{v} \frac{\partial \bar{v}}{\partial x} + \hat{w} \frac{\partial \bar{v}}{\partial y} \\ = -\frac{\partial \hat{p}}{\partial y} + \frac{1}{Re} \left( \frac{\partial^2 \hat{v}}{\partial y^2} - (\alpha^2 + \beta^2) \hat{v} \right) + \hat{f}_v, \end{aligned} \tag{2.8}$$



$$-i\omega\hat{w} + \bar{u} \left( \frac{\partial\hat{w}}{\partial x} + i\alpha\hat{w} \right) + \bar{v} \frac{\partial\hat{w}}{\partial y} = -i\beta\hat{p} + \frac{1}{Re} \left( \frac{\partial^2\hat{w}}{\partial y^2} - (\alpha^2 + \beta^2)\hat{w} \right) + \hat{f}_w, \quad (2.9)$$

where the variables have been non-dimensionalized by a reference length,  $\ell_r$ , and velocity,  $U_r$ , scale such that  $Re = U_r\ell_r/\nu$ . These are essentially the three-dimensional PSE, where the neglected terms include all those involving  $\partial_{xx}()$ ,  $d_x\alpha$  and  $\alpha\partial_x()$ . Writing the above equations in matrix operator form yields

$$\mathbf{A}\hat{q} + \mathbf{B}\frac{\partial\hat{q}}{\partial x} + \mathbf{C}\frac{\partial\hat{q}}{\partial y} + \mathbf{D}\frac{\partial^2\hat{q}}{\partial y^2} = \mathbf{E}\hat{f}, \quad (2.10)$$

which represents a parabolized system in the streamwise direction amenable to a marching solution. Equations (2.10) are solved subject to an initial condition  $\hat{q}(x_0) = \hat{q}_0$  with boundary conditions

$$y = 0 : \hat{u} = \hat{v} = \hat{w} = 0, \quad (2.11)$$

$$y \rightarrow \infty : \hat{u} = \hat{w} = \hat{p} = 0, \quad (2.12)$$

and specified forcing  $\hat{f}$ . The coefficient matrices in (2.10) are defined in appendix A. We note the amplitude functions for the turbulent forcing  $\hat{f}$  arise from the quadratic nonlinearity in (2.3). In general, this internal forcing is unknown as it depends on the fluctuating field and the interaction among wavenumbers. However, for a prescribed wavenumber combination, equation (2.10) describes a linear sub-system of the full Navier–Stokes equations relating the system response  $\hat{q}$  to a specific forcing amplitude  $\hat{f}$  (McKeon & Sharma 2010; McKeon, Sharma & Jacobi 2013; Moarref *et al.* 2013; Beneddine *et al.* 2016).

## 2.2. Solution of the linear sub-system

Upon replacing the wall-normal derivatives by their discrete counterpart, equation (2.10) may be written in semi-discrete form as the generic state-space equation,

$$\frac{\partial\hat{q}}{\partial x} = \mathcal{A}(x)\hat{q} + \mathcal{B}(x)\hat{f}, \quad (2.13)$$

where we refer to  $\mathcal{A}$  as the dynamics matrix and  $\mathcal{B}$  the forcing matrix. Equation (2.13) represents a linear, non-autonomous and non-homogeneous differential equation for the fluctuation amplitude functions  $\hat{q}$  subject to a specified forcing  $\hat{f}$ . Initially, we may consider the homogeneous solution to (2.13), which satisfies the unforced equation  $\partial_x\hat{q} = \mathcal{A}\hat{q}$ . As the system is linear, the homogeneous solution may be written as the linear mapping,

$$\hat{q}(x) = \Phi(x, x_0)\hat{q}(x_0), \quad (2.14)$$

where  $\Phi(x, x_0)$  is referred to as the state transition, or propagator matrix which maps a given state at  $x_0$  to the current state at  $x$ . The principal focus of the present study is on investigating the dynamics of (2.13) via the state-transition matrix. A review of the properties of  $\Phi$ , in particular for non-autonomous operators, may be found, e.g. in Farrell & Ioannou (1996).

For known  $\Phi$ , the particular solution to the non-homogeneous system (2.13) can then be determined using the method of variation of parameters, such that the complete solution is given by

$$\hat{q}(x) = \Phi(x, x_0)\hat{q}(x_0) + \int_{x_0}^x \Phi(x, \xi)\mathcal{B}(\xi)\hat{f}(\xi) d\xi. \quad (2.15)$$

In this case,  $\Phi(x, \xi)$  (or,  $\Phi(x, \xi)\mathcal{B}(\xi)$ ) is the propagator which maps an input state (forcing) at  $\xi$  to an output at  $x$ , and is referred to as the resolvent, Green's function or impulse response of the system (Luchini & Bottaro 2014). Note that if the dynamics matrix  $\mathcal{A}$  was spatially invariant (i.e.  $\mathcal{A} \neq \mathcal{A}(x)$ ), as would occur if the mean flow  $\bar{u}$  was independent of  $x$ , then  $\Phi(x, \xi)$  would be given directly by the matrix exponential  $e^{\mathcal{A}(x-\xi)}$ . Furthermore, if the streamwise variation in the amplitude function is neglected, the constant wavenumber  $\alpha$  would completely describe the streamwise dependence. As such, equation (2.13) could be directly solved to yield the algebraic mapping  $\hat{q} = -\mathcal{A}^{-1}\mathcal{B}\hat{f}$ . The operator  $-\mathcal{A}^{-1}\mathcal{B}$  is then identical to the resolvent operator for parallel flows McKeon & Sharma (2010) and the current parabolized approach given by (2.15) can be seen as a direct extension to slowly developing mean flows.

### 2.3. Current focus on the homogeneous solution

The full system is characterized by (2.15), including both the response to the internal forcing  $\hat{f}$  and the downstream response to the initial state  $\hat{q}(x_0)$ . It is common in linear stability theory to consider the system initially at rest, such that  $\hat{q}_0 = 0$  and examine the long-term state response subject to the harmonic forcing  $\hat{f}$ . In (2.15), however, the initial condition is defined in space as opposed to time. Furthermore, it is not our intention to model the boundary layer through laminar and transitional stages: the boundary layer is assumed turbulent originating from a virtual origin  $x_{vo}$ . At a given downstream position  $x_0 > x_{vo}$ , the fluctuation amplitude  $\hat{q}(x_0)$  is surely non-zero and the homogeneous solution should not be neglected. It implicitly accounts for the cumulative effect of forcing upstream of  $x_0$  that is not explicitly modelled in (2.15). Moreover, as the sub-system given specified forcing amplitude is linear, we may analyse each term in (2.15) independently. In this study, we focus on the homogeneous solution and the dynamics of the state-transition matrix  $\Phi(x, x_0)$ .

As formulated in §2.4, a direct connection may then be made between the present analysis and the theory of spatial optimal disturbances (Andersson *et al.* 1999; Luchini 2000). The main differences between these approaches are that here we consider a turbulent mean flow as opposed to a laminar base state; we further consider perturbations with non-zero frequency and streamwise wavenumber as to include propagating modes as opposed to purely stationary modes. A related approach for stationary optimal disturbances in turbulent flows has been considered by Uzun *et al.* (2017).

We also note the likely overlap between both terms in (2.15). The boundary layer may be assumed to be convection dominated, such that all disturbances are immediately washed downstream by the mean flow with, on average, no upstream propagation (i.e.  $\alpha > 0$ ). The largest downstream response will then be given by a sufficiently upstream 'forcing'. If the forcing amplitude functions  $\hat{f}(\xi)$  are restricted to a single streamwise plane  $x_0$ , then both terms in (2.15) become equivalent. We may expect that only large-scale fluctuations survive over large streamwise distances. As such, the homogeneous solution can then be seen as a filter in which only large-scale structures with upstream sensitivity are retained.

2.4. Optimal disturbance formulation

Given the solution (2.14), we seek to determine the initial amplitude functions which maximize the downstream state response. To measure the size of the fluctuations, we choose the local kinetic energy

$$E(\mathbf{u}(x)) = \int_0^\infty (|u|^2 + |v|^2 + |w|^2) dy. \tag{2.16}$$

Note the kinetic energy is chosen as it provides both a physically meaningful measure of the fluctuation and it is consistent with the dimension of the internal forcing  $\hat{\mathbf{f}}$ , which only operates on the velocity components. We then define  $\hat{\mathbf{u}} = \mathbf{R}\hat{\mathbf{q}}$ , or

$$\begin{pmatrix} \hat{u} \\ \hat{v} \\ \hat{w} \end{pmatrix} = \begin{pmatrix} 1 & 0 & 0 & 0 \\ 0 & 1 & 0 & 0 \\ 0 & 0 & 1 & 0 \end{pmatrix} \begin{pmatrix} \hat{u} \\ \hat{v} \\ \hat{w} \\ \hat{p} \end{pmatrix}, \tag{2.17}$$

where  $\mathbf{R}$  is a restriction operator to eliminate the pressure term from the full state vector. Similarly, the velocity vector may be mapped to the full dimension of the state vector using the prolongation operator  $\mathbf{P}\hat{\mathbf{u}}$  for  $\mathbf{P} = \mathbf{R}^T$ . Equation (2.16) then defines the energy norm and associated scalar product as  $E(\hat{\mathbf{u}}) = \|\hat{\mathbf{u}}\|^2 = \langle \hat{\mathbf{u}}, \hat{\mathbf{u}} \rangle$ .

Following Beneddine *et al.* (2016), we define an arbitrary velocity state  $\psi(x_0)$ , for which the downstream velocity response is given by (2.14) as  $\psi(x) = \mathbf{R}\Phi(x, x_0)\mathbf{P}\psi(x_0) \equiv \Phi_u\psi(x_0)$ . The amplification, or gain  $G$ , from  $\psi(x_0)$  to  $\psi(x)$  is then defined as

$$G = \frac{\|\psi(x)\|^2}{\|\psi(x_0)\|^2} = \frac{\|\Phi_u\psi(x_0)\|^2}{\|\psi(x_0)\|^2} = \frac{\langle \Phi_u\psi(x_0), \Phi_u\psi(x_0) \rangle}{\langle \psi(x_0), \psi(x_0) \rangle} = \frac{\langle \Phi_u^\dagger \Phi_u \psi(x_0), \psi(x_0) \rangle}{\langle \psi(x_0), \psi(x_0) \rangle} \tag{2.18}$$

for  $\Phi_u^\dagger$  the adjoint operator of  $\Phi_u$ . The so-called optimal disturbance that leads to maximum amplification,  $G_{max}$ , over all possible  $\psi(x_0)$ , is identified by the solution of the optimization problem

$$G_{max}(x) = \max_{\psi(x_0)} \frac{\langle \Phi_u^\dagger(x, x_0)\Phi_u(x, x_0)\psi(x_0), \psi(x_0) \rangle}{\langle \psi(x_0), \psi(x_0) \rangle} \tag{2.19}$$

given by the leading eigenvector of  $\Phi_u^\dagger\Phi_u\psi_j(x_0) = G_j\psi_j(x_0)$ . In the following, we assume the eigenvectors  $\psi_j(x_0)$  have been normalized such that  $\|\psi_j(x_0)\|^2 = 1$  and sorted in descending order, such that  $g_1^2 \geq g_2^2 \geq \dots$  where  $g_j^2 \equiv G_j$ . The corresponding optimal response, also normalized, can be determined as  $g_1\psi_1(x) = \Phi_u\psi_1(x_0)$ .

The question then arises as to how well the optimal response  $\psi_1(x)$  approximates the full system response amplitude functions  $\hat{\mathbf{u}}(x)$ . Following McKeon & Sharma (2010), Beneddine *et al.* (2016), we note the operator  $\Phi_u^\dagger\Phi_u$  is Hermitian and, as such, the eigenvectors  $\psi_j(x_0)$  may be chosen as an orthonormal basis for  $\hat{\mathbf{u}}(x_0)$  such that

$$\hat{\mathbf{u}}(x_0) = \sum_j a_j\psi_j(x_0), \quad a_j = \langle \psi_j(x_0), \mathbf{R}\hat{\mathbf{q}}(x_0) \rangle. \tag{2.20}$$

Using the relation  $g_j\psi_j(x) = \Phi_u\psi_j(x_0)$ , the velocity response amplitude functions may be written as

$$\hat{\mathbf{u}}(x) = \Phi_u\hat{\mathbf{u}}(x_0) = \sum_j a_jg_j\psi_j(x). \tag{2.21}$$

Note the  $\psi_j(x)$  also form an orthonormal basis for the velocity response, as shown by the singular value decomposition of  $\Phi_u = \sum_j \psi_j(x) g_j \psi_j^H(x_0)$ . Using (2.21), if  $g_1 \gg g_2 \geq g_3 \dots$  we may consider the velocity response to be approximated by only the first response mode, the so-called rank 1 approximation:

$$\hat{u}(x) \approx \langle \psi_1(x_0), \mathbf{R}\hat{q}(x_0) \rangle g_1 \psi_1(x). \quad (2.22)$$

As shown by Beneddine *et al.* (2016), the approximation holds globally (in an  $L_2$  sense) provided

$$g_1^2 |\langle \psi_1(x_0), \mathbf{R}\hat{q}(x_0) \rangle|^2 \gg \sum_{j \geq 2} g_j^2 |\langle \psi_j(x_0), \mathbf{R}\hat{q}(x_0) \rangle|^2, \quad (2.23)$$

which states that the optimal disturbance, or leading response mode, must capture the dominant portion of the total kinetic energy and the initial state must not be well aligned with any of the sub-optimal modes  $\psi_j(x_0), j \geq 2$ . The first of these conditions is easily verified by examining the computed eigenvalues  $g_j^2$ . The second condition, however, stands as a plausible assumption that can be verified *a posteriori* with experimental comparison.

As shown in §4, the leading eigenvalue  $g_1^2$  corresponding to the optimal disturbance generally contains a dominant fraction of the total energy at a particular wavenumber/frequency combination. This result, consistent with previous resolvent-based approaches (McKeon & Sharma 2010; Moarref *et al.* 2013), indicates the linear sub-system is highly selective, or the linearized Navier–Stokes equations about the turbulent mean acts as a strong directional amplifier. In fact, the shape of the input forcing, or initial condition, is largely inconsequential so long as there is some non-zero component in the direction of  $\psi_1(x_0)$ . Virtually any input, e.g. randomized, will tend towards the ‘optimal’ output and a power iteration approach to solving (2.19) converges extremely fast. In what follows, similar to previous gain-based studies, we consider inputs  $\psi(x_0)$  of unit integrated kinetic energy across all frequencies and wavenumbers and examine purely the inherent amplification of the linear operator. That is, in the rank 1 approximation (2.22), we do not consider the weighting  $a_1 = \langle \psi_1(x_0), \mathbf{R}\hat{q}(x_0) \rangle$  or rather assume  $a_1 = 1$ . Of course, this is not the case in practical turbulent flows, in particular across all parameter combinations. As such, we can expect only qualitative agreement in the amplitude shape functions and computed amplification spectrum. Knowledge of the response  $\hat{u}$  at one or more locations can be used to improve the approximation (Moarref *et al.* 2013; Beneddine *et al.* 2016), however this is not considered.

### 2.5. Method for determining the streamwise wavenumber

We now return to the method for updating the streamwise wavenumber introduced in §2.1. To enforce a slow variation in  $\hat{q}$  of the order of the mean flow, the classical PSE approach imposes an auxiliary equation that enforces the kinetic energy of the shape function be independent of  $x$  (Herbert 1997). This auxiliary equation removes the ambiguity associated with (2.4) and provides a method to iteratively compute the local streamwise wavenumber  $\alpha(x)$ . However, this is designed as a natural extension to normal modes analysis, with the initial condition generally specified as a local eigenmode. As such, the classical PSE formulation is appropriate to study the streamwise evolution of a modal disturbance in which the spatial growth is specified by a local exponential growth rate  $\alpha_i(x)$ .

In the present approach, we do not seek a conventional modal description of the fluctuation amplitudes such that non-modal growth is also captured. The objective is to determine the initial  $\hat{q}(x_0)$  which maximizes the downstream response rather than choosing a local eigenmode and studying its downstream evolution. The streamwise wavenumber is then specified as a real parameter and chosen such that the kinetic energy (2.16) is maximized. Note that  $\alpha(x)$  is chosen locally as part of the downstream marching procedure such that for each discrete streamwise plane  $x_j$ ,  $\alpha(x_j)$  is chosen as that which maximizes  $\langle \psi(x_j), \psi(x_j) \rangle$ . In this manner, this inner optimization procedure for  $\alpha$  may be seen as an auxiliary constraint such that streamwise oscillations are captured in the exponential term of (2.4) and the growth at a particular wavenumber/frequency combination are captured in the amplitude response functions  $\psi(x)$ . As the mean flow varies only slowly with  $x$ , and in the absence of strong modal growth, this implies  $\alpha$ ,  $G$  and hence  $\psi$  also vary slowly with  $x$ . As noted by Tempelmann *et al.* (2010), in which spatial growth was also absorbed into the amplitude functions with real  $\alpha$ , this approach is limited to non-modal and moderate exponential growth. Modes exhibiting strong exponential growth may violate the slowly varying approximation used in the parabolization step.

The current iteration procedure for  $\alpha$  naturally enforces  $\alpha \rightarrow 0$  as  $\omega \rightarrow 0$ . As such, for stationary modes with  $\omega = 0$ , the method is equivalent to conventional spatial optimal disturbances (i.e. Andersson *et al.* (1999)). It also follows that, for propagating modes, the optimal streamwise wavenumber is induced by the mean flow and the  $(\omega, \beta)$  pair, rather than treated as an independent parameter in the resolvent analysis of McKeon & Sharma (2010), Moarref *et al.* (2013). Details of the numeric implementation are given in the following section.

## 2.6. Computational approach

In (2.10), the wall-normal direction is discretized using a spectral collocation method based on Chebyshev polynomials. The Chebyshev collocation points, defined on the interval  $[-1, 1]$ , are mapped to the physical domain  $[0, y_{max}]$  using the rational mapping given by Hanifi, Schmid & Henningson (1996), chosen to cluster points near the centre of the logarithmic region in the turbulent mean flow. The streamwise direction is discretized on a uniform grid over the interval  $[x_0, x_f]$  and the streamwise derivative in (2.10) approximated with a second-order backwards difference. On the first streamwise plane, a first-order scheme is used. Further details of the wall-normal and streamwise discretization are provided in appendix A.

The kinetic energy norm at each streamwise plane may then be written as  $E(\hat{u}) = \|\hat{u}\|^2 = \hat{u}^H \mathbf{M} \hat{u}$  where  $^H$  denotes the conjugate transpose and  $\mathbf{M}$  is a diagonal, positive definite matrix that contains the appropriate quadrature weights (Clenshaw–Curtis) and grid metrics. For known state-transition matrix  $\Phi(x_f, x_0)$ , the discrete solution to the optimization problem (2.19) is readily obtained by solving the eigenvalue problem

$$G\psi(x_0) = (\mathbf{M}_{x_0}^{-1} \Phi_u^H(x_f, x_0) \mathbf{M}_{x_f} \Phi_u(x_f, x_0)) \psi(x_0), \quad (2.24)$$

where the leading eigenvector is referred to as the optimal disturbance with amplification  $G_{max}$ .

As previously discussed, because of the spatial development of the mean flow, the operator  $\mathcal{A}$  in (2.13) is non-autonomous and a general form of state-transition matrix cannot be expressed by standard functions (e.g. the matrix exponential). The alternative is to either directly compute a numerical approximation to the

state-transition matrix, after which  $\Phi_u^H$  is readily computed, or to adopt an iterative approach by which the action of  $\Phi_u$  and  $\Phi_u^H$  are computed by integration of the forward and adjoint equations. The latter avoids direct computation and storage of the state-transition matrix and is the approach taken, for example, by Andersson *et al.* (1999) and Luchini (2000) in computing optimal disturbances in the Blasius boundary layer. A similar approach is followed here, slightly modified to compute the optimal streamwise wavenumber as part of the marching procedure. We also note this adjoint approach is trivially extended to the case where  $\hat{f} \neq 0$ . The adjoint equations are given in appendix B, derived by formulating the optimization problem as one of optimal control theory and driving to zero all variations in the corresponding Lagrange functional. The adjoint implementation was verified by comparing to the direct approach, by approximating  $\Phi_u$ , for stationary disturbances and the current code has been verified in Uzun *et al.* (2017) with the results of Andersson *et al.* (1999). It should be mentioned the direct approach is only applicable for stationary disturbances due to the inner optimization for the streamwise wavenumber. It is also verified in §4 that the retrieved optimal disturbance contains a dominant fraction of the total kinetic energy such that the current rank 1 approximation is valid.

The full optimization procedure utilizing the adjoint approach, including the determination of the local streamwise wavenumber, can be summarized as follows:

- (i) Specify  $\beta$ ,  $\omega$ , the initial plane  $x_0$ , the final plane  $x = x_f$  (specified in terms of  $Re_{\delta^*}$ ) and an initial guess,  $\alpha_0$ . The initial condition  $\psi(x_0)$  is initialized as a random vector.
- (ii) Solve the forward equations (2.10) (with  $\hat{f} = 0$ ):
  - (1) Solve the discretized system at streamwise plane  $x_j$

$$\mathbf{A}_j \psi(x_j) = \mathbf{B}_j \psi(x_{j-1}) + \mathbf{C}_j \psi(x_{j-2}) \quad (2.25)$$

for the local response  $\psi(x_j)$ . The matrices  $\mathbf{A}$ ,  $\mathbf{B}$ ,  $\mathbf{C}$  depend on the local mean flow, the parameters  $\beta$ ,  $\omega$ , and the local estimate for  $\alpha(x_j)$ . Note, on the first marching plane, a first-order version of the discretized system is solved.

- (2) Evaluate the auxiliary constraint  $G = \langle \psi(x_j), \psi(x_j) \rangle = \psi^H(x_j) \mathbf{M}_{x_j} \psi(x_j)$ .
- (3) Update the estimate of the local streamwise wavenumber  $\alpha(x_j)$  based on  $G$  and  $\partial G / \partial \alpha$ .
- (4) Repeat steps (1)–(3) until convergence of  $G$  and/or  $\alpha(x_j)$  within specified tolerance.
- (5) Increment  $j$  and repeat until the final plane  $x_f$ .
- (iii) Obtain the initial condition to the adjoint equation using  $\psi(x_f)$  according to (B 10)–(B 12).
- (iv) Solve the adjoint equations (B 7) from  $x_f$  to  $x_0$ .
- (v) Obtain a new estimate for the initial condition (optimal input disturbance)  $\psi(x_0)$  using the adjoint state at  $x_0$  and (B 13)–(B 15).
- (vi) Repeat steps 2–5 until the relative tolerance in  $G(x_f)$  is below a specified value.

The inner optimization with respect to the local streamwise wavenumber is performed using a quasi-Newton line search algorithm. Depending on Reynolds number, the number of collocation points used in the wall-normal direction ranges from  $N_y = 150$ –300. In the streamwise direction,  $N_x = 100$  points are used. To avoid any low Reynolds number effects in the specification of the mean flow (see §2.8) the



minimum initial plane is taken as  $x_0 = 0.1x_f$ . In select cases, the location of the input plane is also examined, where  $x_0$  is varied in 20 logarithmically spaced points ranging from  $x_f - x_0 = 0.9x_f$  to  $x_f^+ - x_0^+ = 10$  where  $+$  denotes scaling based on inner units. In the results presented below, all variables have been scaled by reference length scales at the final output plane  $x_f$ , e.g. boundary layer thickness  $\delta \equiv \delta_f$  is defined as that  $x_f$ .

### 2.7. Comments on the amplification mechanisms

The downstream marching procedure to solve (2.10) involves essentially the inverse of the coefficient matrices (see also appendix A). These matrices include the local mean flow  $\bar{u}$  and the parameters  $\alpha, \beta, \omega$ . Of these, only the  $\mathbf{A}$  matrix is ‘tuneable’ by the specification of wavenumber/frequency. From a numerical point of view, the gain over a given  $\Delta x$  will become large when the diagonal terms of  $\mathbf{A}$  become small. For large  $Re$ , the viscous contribution may always be assumed small, though not negligible. Therefore, as with a parallel resolvent analysis, we may anticipate large amplifications for  $\alpha = \omega = 0$ , or when the convective term is balanced such that  $(\alpha\bar{u} - \omega) \rightarrow 0$ .

The first of these conditions corresponds to the stationary disturbances of streamwise velocity streaks classically identified in optimal disturbance theory. In this case, amplification is determined by the off-diagonal terms, dominantly the spanwise wavenumber  $\beta$  and the streamwise velocity shear  $\partial_y \bar{u}$ . The physical mechanism by which the corresponding structures amplify is generally attributed to the lift-up effect (Ellingsen & Palm 1975; Landahl 1980) by which three-dimensional disturbances act in regions of high mean shear to induce large streamwise velocities. As noted by Luchini (2000) in the Blasius boundary layer, these structures are necessarily static. For a purely convective mean flow (i.e. no reverse flow, separation, etc.), global oscillations of stationary disturbances, such as those generated by  $\omega \neq 0$  but with  $\alpha = 0$ , would tend to disrupt the amplification process by the lift-up effect. In the present context of a turbulent mean flow, these stationary disturbances can help guide passive control strategies, as in Pujals, Depardon & Cossu (2010), and hence provide valuable information regarding preferential scaling. In describing turbulent fluctuations, however, these stationary disturbances are somewhat ambiguous as they do not contribute to the fluctuation energy and naturally observed structures are convective. Their relation to real turbulent structures is often accompanied by a secondary instability mechanism describing the breakdown to convective disturbances.

The second condition for large amplification corresponds to so-called critical layer behaviour when the phase velocity of the fluctuation matches that of the local mean, or  $\omega/\alpha = \bar{u}$  such that the diagonal terms of  $\mathbf{A}$  are minimized. Note the critical layer behaviour is naturally enforced in an integral sense, as the fluctuation is distributed in the wall-normal direction. This concept is also related to the convective non-normality described by Marquet, Lombardi & Chomaz (2009). The most amplified fluctuation can be seen as that which is optimally transported by the mean flow. As these structures are naturally convective, we expect them to better represent the natural structures observed in turbulent boundary layers. Furthermore, because of this convective nature, the downstream response will be most sensitive to an upstream condition, such that the spatial development of the mean flow will play a prominent role in the selection of the optimal response. The present formulation is then well equipped to identify these structures.

### 2.8. Turbulent boundary layer mean flow

The solution of (2.10) requires only the specification of the turbulent boundary layer mean flow profile and its gradients at each streamwise position. In the current study,

this is modelled using the self-consistent, composite profile proposed by Monkewitz, Chauhan & Nagib (2007) for high Reynolds number, zero-pressure-gradient turbulent boundary layers. The composite profile follows a classical scaling of inner, outer wake and logarithmic overlap layers locally given by

$$\frac{\bar{u}(y)}{u_\tau} = U_{inner}^+(y^+) - U_{log}^+(y^+) + U_\infty^+(Re_{\delta^*}) - W_{outer}^+(\eta), \quad (2.26)$$

where  $u_\tau = (\tau_w/\rho)^{1/2}$  is the wall friction velocity,  $y^+ = yu_\tau/\nu$  is the viscous wall unit (inner coordinate),  $U_\infty^+$  is the free-stream velocity scaled by  $u_\tau$ ,  $Re_{\delta^*}$  is the Reynolds number based on displacement thickness  $\delta^*$ , and  $\eta = y/\Delta$  is the outer coordinate, or the wall-normal coordinate scaled by the Rotta–Clauser length scale  $\Delta = U_\infty^+\delta^*$ . Note in the description of the mean flow by Monkewitz *et al.* (2007),  $\Delta$  is taken as the outer length scale. Although not strictly constant, the conventional 99% boundary layer thickness  $\delta$  is roughly  $0.22\Delta$ . This also defines the friction Reynolds number as  $Re_\tau \approx 0.22Re_{\delta^*}$ . In the current study, we typically use the more familiar boundary layer thickness  $\delta$  as the outer scale to ease comparison with experimental data. The explicit expressions for the terms in (2.26) are provided in Monkewitz *et al.* (2007) and are not repeated here for brevity sake. However, the profiles are shown to fit well to experimental data (e.g. Österlund (1999)) from the wall to the free stream. Monkewitz *et al.* (2007) also provides explicit expressions for the streamwise development of the boundary layer length scales (e.g. the momentum thickness,  $\theta(x)$ ) used to compute the spatially evolving mean flow. Cossu *et al.* (2009) provides additional relations to compute the wall-normal velocity component and corresponding mean flow gradients.

Though not explicit in (2.26), the streamwise coordinate  $x$  is defined with respect to the virtual origin such that the boundary layer is assumed to be fully developed with self-similar inner and outer mean velocity profiles, from  $x=0$  onward. While this may not represent a physical location in real flows, it provides a sensitive metric of the quality of turbulent boundary layer data in that a given experiment should produce the same virtual origin at various streamwise measurement stations. As such, it represents an equivalent development length insensitive to the genesis of the boundary layer. We also note that the same profile was used in the temporal optimal disturbances of Cossu *et al.* (2009), although under the parallel flow approximation. Sample profiles of the turbulent mean flow at various Reynolds numbers investigated in the current study are shown in figure 1.

### 3. Steady, streamwise elongated optimal disturbances

In accordance with previous optimal disturbance studies on both laminar and turbulent flows, we limit our initial discussion to the development of steady, streamwise elongated streaks of  $\alpha = \omega = 0$  with spanwise wavenumber  $\beta$ , discussed in § 2.7. These are generally recognized as the global optimum in terms of amplification, although this is shown in § 4 not to be the case for present study. Nonetheless, these steady disturbances are significantly amplified and provide valuable scaling information regarding the selection of preferential scales by the turbulent mean flow and the effect of streamwise development in a condensed parameter space.

To examine the spatial development of optimal disturbances in the turbulent boundary layer where a separation of scales is known to occur, at least for high enough Reynolds number, it is also necessary to examine the relation between input/output plane and spanwise wavenumber. We may expect the spanwise wavelength

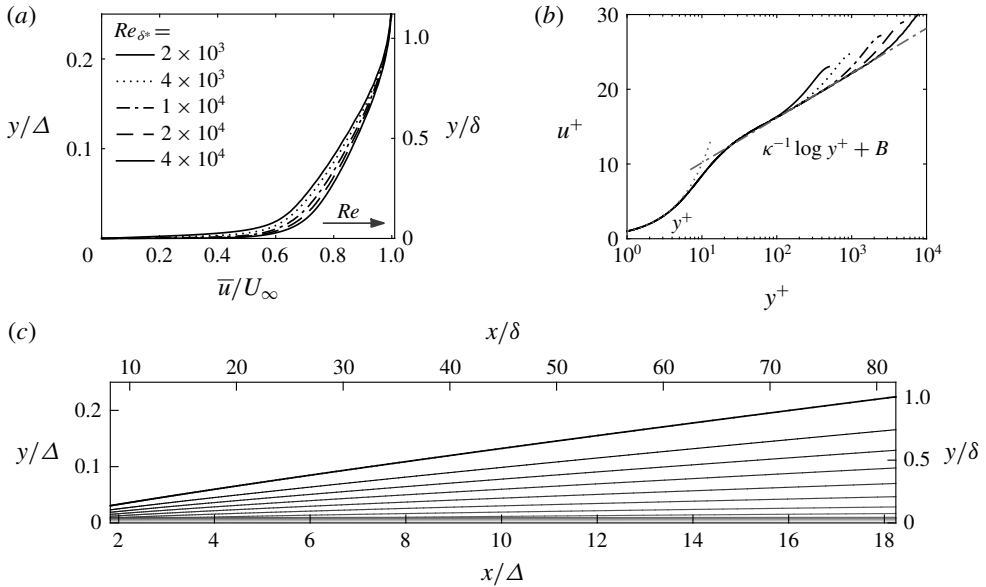


FIGURE 1. Turbulent boundary layer profiles for various Reynolds number,  $Re_{\delta^*}$ , for (a) the mean flow plotted in outer units, (b) the mean flow plotted in inner units, with the linear sublayer and logarithmic layer denoted and (c) the spatial development of the turbulent boundary layer mean flow from  $Re_{\delta^*} = 2 \times 10^3$  to  $Re_{\delta^*} = 2 \times 10^4$ . The contour levels are 20 evenly spaced increments from  $\bar{u}/U_\infty = 0.1$  to 0.99 (i.e. the upper contour denotes the 99% thickness). Note in (c) the  $x$  and  $y$  axes are not scaled equally for visualization purposes. Both  $\Delta$  and  $\delta$  scaling is shown for comparison.

of the disturbance be proportional to the separation distance between input and output plane corresponding effectively to a scale-dependent disturbance ‘lifetime’. To examine this dependence, while evaluating the optimals at the same streamwise location, the output is fixed at a prescribed  $x_f$  defined by  $Re_{\delta^*}$ . The input plane is then varied from near virtual origin of the turbulent boundary layer,  $x_0 = 0.1x_f$ , to very short separation distances,  $x_f^+ - x_0^+ = 10$ , over which the mean flow may be considered essentially parallel. This range is then discretized into 20 logarithmically spaced streamwise positions, and for each separation distance  $x^*$  the optimal disturbance computed for varying  $\beta$ .

The optimization results for a moderately high  $Re_{\delta^*} = 2 \times 10^4$  ( $Re_\tau = 4460$ ) are reported in figure 2(a), in which the wavenumber sweep at each streamwise position represents a slice from a surface of optimal energy amplification. Note all length scales have been normalized by boundary layer thickness at the output plane  $x_f$ . As expected, the range of amplified wavenumbers directly corresponds to the separation between input/output planes. For the smallest  $x^*$ , only the highest wavenumbers are amplified. Increasing  $x^*$  leads to a decrease in the local optimal  $\beta$ , or increase in  $\lambda_z$ . This is accompanied by a monotonic increase in the local maximum amplification, such that the most amplified wavenumbers are achieved for the largest  $x^*$ , or disturbances generated farthest upstream. Because disturbances are transient, the longer the separation distance the larger the required disturbance to maximize amplification far downstream. Smaller scales are amplified faster, but also rapidly decay due to viscous diffusion.

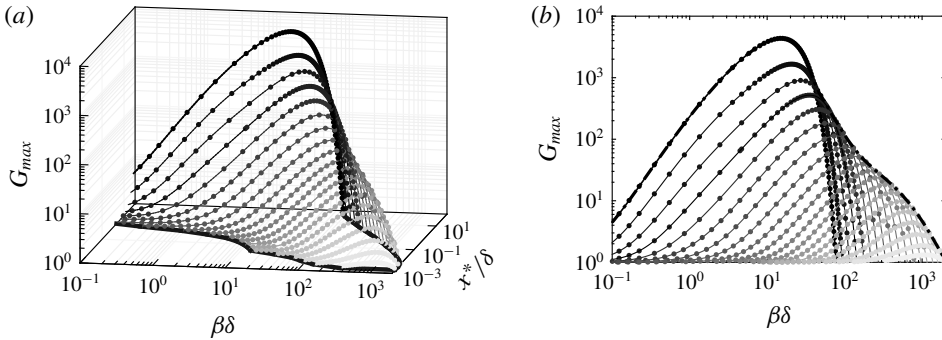


FIGURE 2. (a) The surface of optimal energy amplification for steady, streamwise elongated ( $\alpha = \omega = 0$ ) disturbances as a function of spanwise wavenumber and streamwise separation distance  $x^* = x_f - x_0$ , computed for  $Re_{\delta^*} = 2 \times 10^4$ . The colour scale indicates the streamwise separation of the input/output plane, with light to dark representing short to long separation, respectively. The thick line in the  $\beta$ - $x$  plane is the isocontour of  $G_{max} = 1$ , outside of which no energy amplification occurs. (b) The projection into the  $\beta$ - $G_{max}$  plane, with the dash-dotted line indicating the spatial envelope of maximum energy amplification over all streamwise separations at each spanwise wavenumber.

For each streamwise separation distance, there is a relative band of spanwise wavenumbers which are amplified. Outside of which, the energy of any input disturbance has decayed below its initial value, although this spatial decay is not necessarily monotonic. This region is denoted in figure 2(a) by the dashed line at the intersection of the local amplification spectrum with the  $G_{max} = 1$  plane. At a given  $Re_{\delta^*}$ , however, we expect the cumulative effect of all upstream disturbances such that the full spectrum of amplification is given by projection of figure 2(a) into the  $\beta$ - $G_{max}$  plane. This is equivalent to further optimizing the amplification at  $x_f$  with respect  $x_0$  and analogous to temporal optimal disturbances in which the optimization is generally performed for all time (see, for example, Schmid & Henningson 2001). This projection is shown in figure 2(b), which identifies the spatial envelope of maximum amplification denoted by the dash-dotted line. Here, it is seen that the amplification reaches nearly four orders of magnitude at the peak wavenumber  $\beta\delta \approx 15.6$ , corresponding to  $\lambda_z \approx 0.4\delta$ . This peak, however, is quite broad and a wide range of wavenumbers achieve appreciable energy amplification, spanning wavelengths from several times to less than 1% of the boundary layer thickness.

To investigate the Reynolds number effect on the steady optimal disturbances, we compute the spatial envelopes for varying Reynolds number ranging from low, in which the mean flow lacks an appreciable logarithmic layer, to moderately high values with a well developed logarithmic layer and expected separation of scales (see figure 1b). These results are presented in figure 3 in which the envelopes for each  $Re_{\delta^*}$  show a single, dominant peak in maximum energy amplification. We also note that, although not shown, in each case the maximum amplification occurs for the farthest upstream  $x_0$ . For each  $Re_{\delta^*}$ , both amplitude and spanwise wavenumber increase with Reynolds number. This indicates, contrary to previous temporal optimal disturbance results, that the optimal spanwise wavenumber does not scale purely in outer units, e.g. boundary layer thickness. In addition, the range of spanwise scales that are amplified increases accordingly with  $Re_{\delta^*}$ . For  $Re_{\delta^*} \approx 1 \times 10^4$  ( $Re_\tau \approx 2230$ ) and higher, an intermediate region marked by a  $\beta^{-2}$  dependence in the amplification

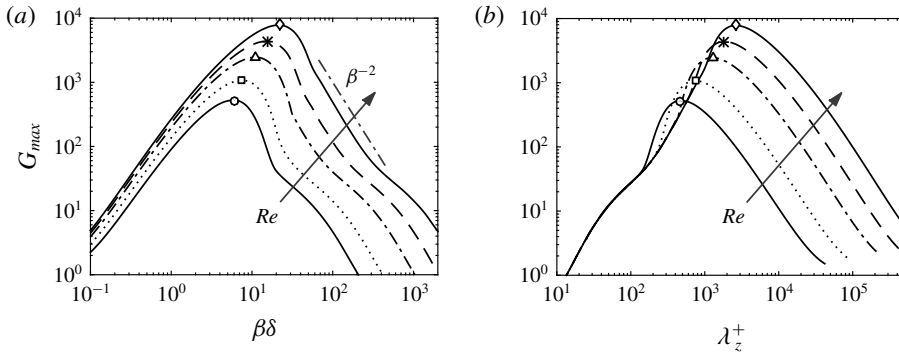


FIGURE 3. The spatial envelope of maximum energy amplification for steady, streamwise elongated disturbances ( $\alpha = \omega = 0$ ), computed for various Reynolds numbers. (a) Outer scaling and (b) inner scaling. The legend is the same as figure 1(a).

spectrum is observed connecting the peak amplification with the high wavenumber decay. This  $\beta^{-2}$  dependence was also observed in the linear analysis of Hwang & Cossu (2010) for harmonic forcing in turbulent channel flow, and was derived from the generalized Orr–Sommerfeld and Squire equations under the assumption of a logarithmic variation of the mean flow and geometrically similar disturbances, i.e.  $y \sim \lambda_z$ . Similar conclusions can be drawn from the scaling analysis of Moarref *et al.* (2013) for self-similar resolvent modes in the log layer with zero streamwise wavenumber. Consistent with these parallel approaches, we note the  $\beta^{-2}$  dependence emerges only at Reynolds numbers high enough for a well-established log layer to emerge in the mean flow. It is worth noting, however, that no such behaviour is observed in the analogous temporal response to initial conditions under the parallel flow approximation (Cossu *et al.* 2009).

To investigate the scaling of the high wavenumber spectrum, the spatial envelopes are plotted in figure 3(b) as a function of spanwise wavelength in wall units. For small wavelengths, an identical collapse is observed with a Reynolds number independent energy amplification. As  $Re_{\delta^*}$  is increased, this region of collapse is extended across higher spanwise wavelengths. For  $\lambda_z^+ \gtrsim 100$  a characteristic change in the amplification is seen. This corresponds to the  $\beta^{-2}$  region of figure 3(a). Structures associated with wavelengths below this threshold are centred approximately in the viscous sub- and buffer layers of the mean flow while those above have their maximum contribution within the log layer for sufficiently high  $Re_{\delta^*}$ .

Noticeably absent, however, in the envelope of figure 3(b) is the presence of a secondary, inner-scaled peak for  $\lambda_z^+ \approx 80$ –100 reported in temporal optimal disturbances of wall-bounded turbulent flows (del Álamo & Jiménez 2006; Cossu *et al.* 2009). Although the envelope spans the appropriate wavenumber range, and displays a characteristic scaling in wall units, the appearance of a secondary ‘inner’ peak is a direct consequence of the scale separation imposed by the use of an eddy viscosity based on the mean flow which is not included in the present model (this is briefly discussed in § 5). As shown below, however, the familiar inner peak is reproduced in the premultiplied streamwise energy density rather than the raw amplification spectrum.

Although not shown, the optimal disturbances corresponding to the amplification in figure 3 form the familiar streamwise velocity streaks well known in non-modal

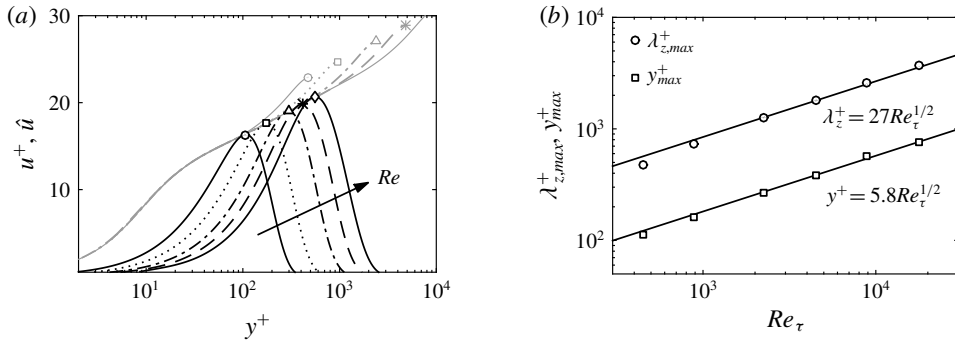


FIGURE 4. (a) The optimal output,  $\hat{u}$ , corresponding to the peak spanwise wavenumber in figure 2 for increasing Reynolds number. The mean flow is also plotted in grey to illustrate the location of the disturbance at the approximate centre of the logarithmic region. The legend is the same as figure 1(a). (b) The variation in optimal spanwise wavelength,  $\lambda_{z,max}^+$ , and its wall-normal maximum,  $y_{max}^+$ , with Reynolds number  $Re_\tau$ . The solid lines indicate a best fit to  $Re_\tau^{1/2}$ . Note an additional Reynolds number of  $Re_{\delta^*} = 8 \times 10^4$  ( $Re_\tau \approx 17\,800$ ) was included to verify the identified scaling.

stability theory for both laminar and turbulent flows (e.g. Andersson *et al.* 1999). The associated input disturbances consist predominantly of wall-normal and spanwise velocity components forming counter-rotating vortices, with essentially negligible streamwise component. However, at the output, only the streamwise disturbance component is appreciably amplified.

### 3.1. Scaling of the optimal spanwise wavenumber

Aside from the absence of a secondary peak in figure 3, the most substantial result is the apparent lack of outer scaling in the spanwise spectrum as the optimal spanwise wavenumber shifts to higher values for increasing Reynolds number. In terms of outer units, this requires the optimal structures to decrease in spanwise wavelength with respect to the local boundary layer thickness. To examine the scaling of the peak wavenumber, the streamwise component of the optimal disturbance is plotted alongside the mean flow in figure 4(a) for various Reynolds number. Note the disturbance velocity has been scaled to match the mean flow for graphical clarity. The wall-normal location of peak disturbance velocity, denoted as  $y_{max}^+$ , clearly increases with increasing Reynolds number when scaled in viscous units. Further, these profiles are approximately similar in the scaling  $y/y_{max}$ . Interestingly, the increase in the inner-scaled wall-normal position of the optimal disturbance is aligned with the increase in the extent of the logarithmic overlap in the mean flow, with the peak disturbance velocity occurring near the centre of the log layer. This result is consistent with the scaling of VLSMs and superstructures observed experimentally in turbulent boundary layers, where Mathis *et al.* (2009) showed the outer peak in the premultiplied streamwise energy spectra occurred near the geometric mean of the log region. Assuming fixed lower and upper bound estimates for the log region of  $y^+ > 100$  and  $y/\delta < 0.15$  respectively, or  $100 < y^+ < 0.15Re_\tau$ , the geometric mean increases as  $y_c^+ \sim 3.9Re_\tau^{1/2}$ .

In figure 4(b), the variation of the optimal spanwise wavelength, corresponding to maximum amplification in figure 3(b), and wall-normal location of maximum



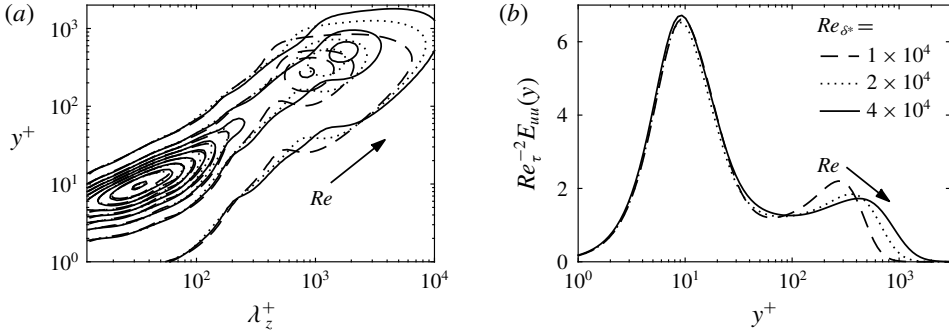


FIGURE 5. (a) Premultiplied streamwise energy density, defined by (3.1), obtained from the optimal output disturbance along the envelope of maximum energy amplification and (b) the streamwise energy density integrated over all spanwise wavenumber contributions,  $E_{uu}(y)/Re_\tau^2$ . Only the higher Reynolds number cases are shown,  $Re_\tau \approx 2230, 4460, 8920$ .

disturbance velocity is plotted as a function of  $Re_\tau$ . Both the inner-scaled spanwise wavelength and wall-normal position are well described by a  $Re_\tau^{1/2}$  dependence, denoted by the fit lines in figure 4(b). The location of the maximum disturbance velocity lies just above the estimated centre of the log layer at  $y_{max}^+ \approx 5.8Re_\tau^{1/2}$ . The optimal spanwise wavelength,  $\lambda_{z,max}^+$ , similarly increases as  $\sim 27Re_\tau^{1/2}$ , leading to constant aspect ratio disturbances with  $\lambda_z \sim 4.7y$ . As expected, the  $Re_\tau^{1/2}$  dependence is strictly observed only for the higher Reynolds number cases. In fact, for the lowest Reynolds number  $Re_\tau \approx 446$ , the upper bound of the estimated log region,  $y > 0.15\delta$ , lies below the lower bound of  $y^+ > 100$  such that no log layer can be said to exist. As noted by Hutchins & Marusic (2007b), the overlap between these two positions occurs for  $Re_\tau \gtrsim 667$  such that an appreciable log layer occurs only for significantly higher  $Re_\tau$ . This is reflected in the scaling observed in figure 4(b).

### 3.2. Identification of energetic spanwise structure

To determine the spanwise structure with the largest contribution to the total disturbance energy, we use the streamwise component of the optimal disturbance response to construct a rank 1 approximation to the streamwise energy density as a function of spanwise wavenumber. The premultiplied streamwise energy density for stationary disturbances is then defined as

$$E_{uu}(y; \beta) = \beta(g_1(\beta)|u_1(y; \beta)|)^2, \quad (3.1)$$

where  $u_1$  is the streamwise velocity of the optimal disturbance response normalized to unit integrated kinetic energy and  $g_1$  is the square root of the mode energy.  $E_{uu}$  is plotted in figure 5(a) as a function of  $\lambda_z^+$ , where only the higher  $Re_{\delta^*}$  cases are shown for clarity. Contrary to the pure amplification spectra in figure 3, figure 5(a) reveals two peaks in the premultiplied streamwise energy density. We refer to these peaks here as the inner and outer peaks, in which the outer peak is associated with the log-layer-scaled structures identified in figure 4. In figure 5(a), however, the dominant contribution to the streamwise energy is from the inner peak. The location of this inner peak is constant in both spanwise wavelength and wall-normal position when scaled in wall units, with the contour levels for all three  $Re_{\delta^*}$  nearly indistinguishable.

Though a direct comparison with streamwise energy of turbulent fluctuations may not be strictly valid as the disturbances here correspond to stationary structures with zero frequency, the scaling of the inner peak in figure 5(a) is consistent with the near wall streaks observed in wall-bounded turbulence. The maximum is seen to occur for  $(\lambda_z^+, y^+) \approx (40, 10)$ , in reasonable agreement with the well accepted near wall streaks of  $\lambda_z^+ \approx 100$  centred at  $y^+ \approx 12$ –15.

The secondary, outer peak contributes less to the overall energy and shifts to both higher spanwise wavelengths and wall-normal positions scaled in inner units. It should be mentioned, this outer peak is only distinguishable from the inner peak for moderately high  $Re_{\delta^*}$ . Similar to the most amplified disturbances shown in figure 4, the location of the secondary peak in the premultiplied streamwise energy density scales with  $Re_{\tau}^{1/2}$ , shifted to slightly smaller positions with  $\lambda_z^+ \approx 20Re_{\tau}^{1/2}$  and  $y^+ \approx 5.5Re_{\tau}^{1/2}$ . The spanwise wavelength and wall-normal position of both the inner and outer peak agree well with the resolvent analysis of Moarref *et al.* (2013) in turbulent channel flow, where the inner peak in the premultiplied streamwise energy density was found to occur at  $(\lambda_z^+, y^+) \approx (44, 11)$  and the middle peak for  $\lambda_z^+ \approx 20Re_{\tau}^{1/2}$  and  $y^+ \approx 5.2$ – $5.8Re_{\tau}^{1/2}$ . Note, however, that the results of Moarref *et al.* (2013) were obtained for traveling wave solutions integrated over all streamwise wavelengths and temporal frequencies and also contained a dominant peak corresponding to large-scale outer layer structures scaling with the channel height. Such outer-scaled structures are not observed here for stationary modes but will be discussed in §4.

Finally, the profile of streamwise energy intensity obtained by integrating over all spanwise wavenumbers in figure 5(a) is shown in figure 5(b). A large peak in the streamwise energy is seen at  $y^+ \approx 10$  with amplitude approximately constant with  $Re_{\tau}^2$ . Similar to figure 5(a), an outer peak is seen for larger  $y^+$  values. The location of this outer peak increases in  $y^+$  with increasing Reynolds number. The amplitude, however, does not scale with  $Re_{\tau}^2$  as the inner peak.

#### 4. Travelling wave optimal disturbances

In this section, we present results for the more general case in which the disturbance frequency, and hence the streamwise wavenumber, is not constrained to zero. This model, as discussed in §2, forms travelling wave disturbances and permits a more physically relevant comparison with natural energetic fluctuations observed in turbulent boundary layers.

In what follows, we restrict the discussion to large-scale disturbances generated far upstream with  $x_0 = 0.1x_f$ . Our focus on these disturbances is twofold. As shown in the previous section, the most amplified disturbances correspond to those generated farthest upstream. Accordingly, these structures are most influenced by the spatial development of the mean flow and hence of particular interest in the present study. As the separation between input/output plane becomes smaller, higher wavenumber disturbances are amplified. In the case of travelling wave disturbances, this translates to higher frequency disturbances with shorter streamwise and spanwise scales. In this manner, the small-scale, inner layer structures are recovered with similar spanwise scaling shown in figure 5(a). However, in the streamwise extent over which these small structures are preferentially amplified, the mean flow is essentially parallel and the results reproduce the scalings observed in similar parallel resolvent-based analyses (e.g. Moarref *et al.* 2013). Considering this, we focus on the disturbances which reveal differences as a consequence of the spatially developing mean flow.

Sample optimization results are shown in figure 6, computed for  $Re_{\delta^*} = 2 \times 10^4$  with  $\beta\delta = 15.6$  and  $\omega\delta/U_{\infty} = 0.223$ . The chosen spanwise wavenumber corresponds to

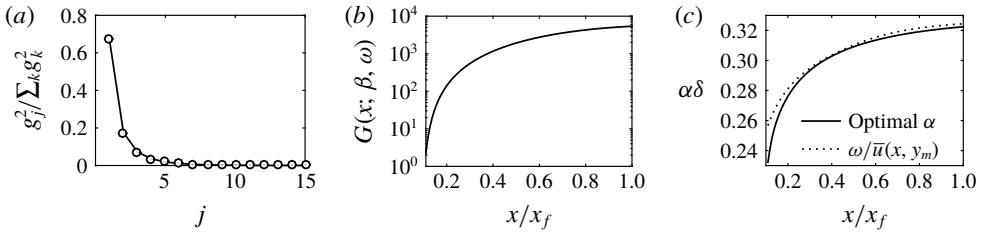


FIGURE 6. Sample results for propagating disturbances, computed for  $Re_{\delta^*} = 2 \times 10^4$  with  $\beta\delta = 15.6$ ,  $\omega\delta/U_\infty = 0.223$ . (a) The relative energy contribution of the first 15 modes ( $j = 1$  referred to here as the optimal disturbance with  $g_1^2 = G_{max}$ ). (b) The streamwise evolution of the energy amplification of the optimal disturbance and (c) the local streamwise wavenumber computed at each  $x$  position, compared with a critical layer approximation  $\alpha = \omega/\bar{u}(x, y_m)$  for  $y_m$  the location where  $|u|$  is maximum.

the peak wavenumber identified from the steady disturbances ( $\omega = 0$ ) in figure 2(b). Figure 6(a) illustrates the relative energy contribution of the first 15 modes, or eigenvalues of (2.24). Note the optimal propagating modes are computed using the iterative approach of the forward and adjoint equations, as discussed in § 2.6, which converges to the leading eigenmode by default. Successive eigenmodes are then computed using a modified Gram-Schmidt orthogonalization procedure, by which the current estimate of the initial condition at  $x_0$  for mode number  $j$  is projected orthogonal to all preceding modes  $1, \dots, j - 1$ . This procedure is continued until the computed eigenvalue is below one, i.e. the modes no longer achieve any energy amplification at the specified output, which occurs for  $j = 16$  in this case. The leading mode  $j = 1$ , or optimal disturbance, dominates all subsequent modes with  $\approx 70\%$  of the total energy amplification. The relative contribution of successive modes decays rapidly. Similar trends were observed for other parameter combinations ( $\beta, \omega$ ). As such, following the discussion of § 2.4, we may consider the optimal disturbance (rank 1 approximation) to be representative of, on average, energetic motions observed in real turbulent flows if there exists an input (feedback) at the particular wavenumber/frequency combination.

The streamwise evolution of the energy amplification for the optimal disturbance ( $j = 1$  in figure 6(a)) is shown in figure 6(b). Similar to the stationary disturbances in § 3, the energy amplification reaches nearly four orders of magnitude at the final output plane  $x_f$ . Note the optimization is performed with respect to the final output plane only, and not the full spatial evolution, such that at  $x_f$ ,  $G(x_f) \equiv G_{max}$ . The corresponding streamwise wavenumber, computed from the inner optimization described in § 2.5, is shown in figure 6(c). A general increase in  $\alpha$  is observed over the streamwise domain, or a decrease in the streamwise wavelength, although this behaviour is not strictly representative of all ( $\beta, \omega$ ) parameter combinations. For reference, the streamwise wavelength at  $x_f$  corresponds to  $\lambda_x \approx 20\delta$ , with phase speed  $c = 0.69U_\infty$ . Plotted alongside the optimized streamwise wavenumber is an estimate using a local critical layer approximation. As discussed in § 2.7, the amplification should be maximized when the disturbance phase velocity matches that of the local mean, or the term  $(\alpha\bar{u} - \omega) \rightarrow 0$ . To illustrate this, in figure 6(c) the ratio  $\omega/\bar{u}(x, y_m)$  is plotted, where  $\bar{u}(x, y_m)$  is the mean streamwise velocity at wall-normal location  $y_m$ , and  $y_m$  the location at which the disturbance streamwise velocity  $|u|$  is maximum. A good agreement is seen between the optimized  $\alpha$  and the critical layer estimate. The two differ most for small

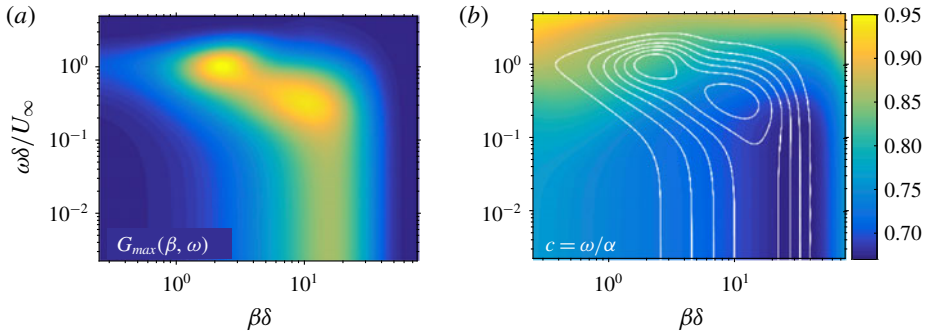


FIGURE 7. (Colour online) (a) Amplification of the optimal disturbance as a function of spanwise wavenumber and radian frequency, computed for  $Re_{\delta^*} = 2 \times 10^4$ . (b) The corresponding phase speed with isocontours of the amplification in (a) are overlaid for reference.

$x/x_f$ , largely due to the fact that the initial disturbance is comprised mainly of wall-normal and spanwise velocity components, with small streamwise velocity used to compute  $y_m$  in the estimate.

In the following, for each parameter combination  $(\beta, \omega)$ , we extract the values of  $G_{max}$  and  $\alpha$  at the final output plane  $x_f$  corresponding to the chosen  $Re_{\delta^*}$ .

#### 4.1. Most amplified propagating modes

To examine the dependence of optimal disturbance amplification on spanwise wavenumber and frequency, these parameters are discretized on logarithmically spaced grids and the procedure outlined in figure 6 computed for each combination. Here, only the leading mode considered. The computations are truncated when the amplification  $G_{max} < 1$ . Results for  $Re_{\delta^*} = 2 \times 10^4$  are plotted in figure 7(a). The  $\lim_{\omega \rightarrow 0} G_{max}$  naturally corresponds to the stationary disturbances discussed in the previous section and the spanwise spectrum at the smallest frequency plotted in figure 7(a) ( $\omega\delta/U_\infty = 0.002$ ) aligns exactly with the amplification spectrum in figure 2(a) for  $x_0 = 0.1x_f$ . This amplification is approximately constant, or independent of  $\omega$ , for  $\omega\delta/U_\infty \lesssim 0.07$ . However, a further increase in frequency leads to an appreciable increase in  $G_{max}$ , such that the global optimum in energy amplification occurs for propagating modes and not the stationary modes discussed in § 3.

In figure 7(a), two distinct peaks in energy amplification are seen in the propagating modes. The first peak (in terms of increasing  $\omega$ ) is observed for a slightly smaller spanwise wavenumber than the corresponding stationary modes, with  $\beta\delta \approx 10$  and  $\omega\delta/U_\infty \approx 0.3$ . For reference this corresponds to a spanwise wavelength of  $\lambda_z \approx 0.6\delta$  and streamwise wavelength, using the computed  $\alpha$  at the output plane, of  $\lambda_x \approx 13.8\delta$ . These values are well aligned with reported structures observed in turbulent boundary layers, in particularly the VLSMs or superstructures identified in instantaneous visualizations. In comparison to the previously discussed steady disturbances, the energy amplification associated with this peak increases by approximately 43%.

The second peak occurring for higher frequency disturbances is the primary, or global, peak in energy amplification at this particular  $Re_{\delta^*}$  with  $\sim 51\%$  increase in amplification over the stationary modes. This occurs for  $\beta\delta \approx 2.2$  and  $\omega\delta/U_\infty \approx 1.0$ , or spanwise and streamwise wavelengths of  $\lambda_z \approx 2.8\delta$  and  $\lambda_x \approx 5.1\delta$ , respectively.

Note the spanwise wavelength associated with this primary peak is significantly larger than the secondary peak, although the streamwise wavelength is much shorter. As such, the aspect ratio  $\lambda_x/\lambda_z$  of these higher frequency disturbances are smaller. The spanwise wavelength leading to maximum amplification is also in good agreement with the spanwise scale of conventional optimal disturbances in Blasius boundary layers ( $\lambda_z \approx 2.8\delta$ ) (Andersson *et al.* 1999), and laminar and turbulent channel flow ( $\lambda_z \approx 3h$ ) (Reddy & Henningson 1993; del Álamo & Jiménez 2006), although those were obtained for stationary disturbances with either infinite or very long streamwise wavelengths.

At this moderate Reynolds number, both peaks are well separated in spectral space. Furthermore, no similarly scaled disturbances were identified in the stationary results such that the corresponding modes appear unique to propagating disturbances. The physical significance of both peaks are discussed in following sections. For frequencies  $\omega\delta/U_\infty \gtrsim 2.2$ , no parameter combination leads to appreciable amplification for the input plane considered,  $x_0 = 0.1x_f$ . It should be noted, however, if the input plane is moved closer to the output, smaller-scale structures (i.e. higher  $\beta$  and  $\omega$ ) are amplified such that the upper contours in figure 7(a) would continue diagonally to the right. As seen in the stationary disturbances, these small-scale structures have much lower amplification, but cover a much larger spanwise wavenumber and frequency range, such that their energy contribution is significant.

Each parameter combination in figure 7(a) is associated with a unique streamwise wavenumber extracted at the final output plane. As such, we plot the disturbance phase velocity,  $c = \omega/\alpha$ , in figure 7(b), with isocontours of amplification overlaid for reference. Here, the two identified peaks are seen to have phase velocities of approximately  $0.7U_\infty$  and  $0.8U_\infty$ , respectively. Similar to the amplification, the phase velocity is approximately constant for fixed  $\beta$  with increasing frequency for  $\omega\delta/U_\infty \lesssim 0.07$ . For higher frequency disturbances, there is a general increase in phase velocity with increasing frequency, and similarly with decreasing spanwise wavenumber. In accordance with Taylor's hypothesis, the disturbances are seen to convect at approximately the local mean evaluated near the disturbance peak streamwise velocity. As  $\omega$  increases, the corresponding disturbance mode shapes (for example, see figures 10 and 11) begin to lift off the wall, with their maximum contribution centred in regions of higher mean flow velocity. A similar behaviour has been noted in McKeon & Sharma (2010). For large  $\omega$  and relatively low  $\beta$ , the mode shapes can be said to become detached from the wall such that they have negligible contribution in the near wall region (figure 11a). These are essentially free-stream modes with their wall-normal maximum occurring either in the wake region of the mean flow, or near the edge of the boundary layer, and denoted with phase velocity  $c \gtrsim 0.8$  in figure 7(b). Conversely, modes with small frequency but large spanwise wavelength have support over a large wall-normal extent such that they maintain high convection velocity.

To examine the Reynolds number scaling, the amplification spectrum in figure 7(a) is computed for varying Reynolds number. Two additional representative cases ranging from low to moderately high  $Re_{\delta^*}$  are shown in figure 8. Note the results of figure 7(a) are reproduced in figure 8(b) for reference. In each case, a peak in amplification is observed for  $\omega > 0$ . This occurs consistently for a slightly lower spanwise wavenumber than for the corresponding stationary optimal. For the lowest  $Re_{\delta^*}$  considered (figure 8a), only a single peak in amplification can be clearly distinguished at  $\beta\delta \approx 2.2$ . This is a direct consequence of the lack of scale separation in the mean flow. The location of this peak with increasing  $Re_{\delta^*}$  is approximately



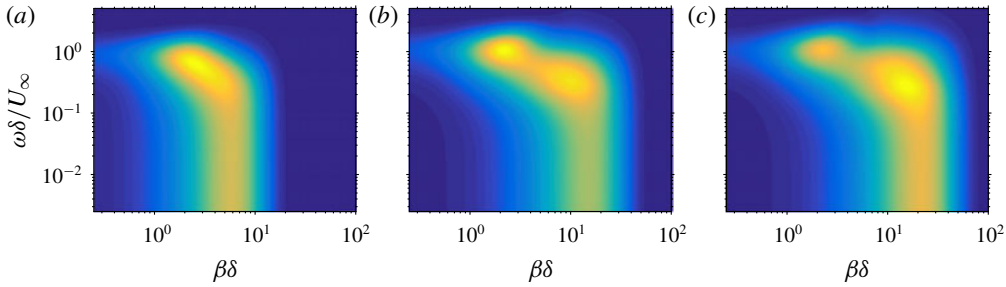


FIGURE 8. (Colour online) Amplification of the optimal disturbance, (a)  $Re_{\delta^*} = 2 \times 10^3$ , (b)  $Re_{\delta^*} = 2 \times 10^4$ , (c)  $Re_{\delta^*} = 4 \times 10^4$ . Note the contour levels are scaled by the maximum amplification for each  $Re$  and are hence not the same.

constant in the outer-scaled spanwise wavenumber, with a slight increase in  $\omega$ . The peak at lower  $\omega$  emerges only for the higher  $Re_{\delta^*}$  cases. Additional cases not shown here indicate the two peaks become distinguishable for  $Re_{\delta^*} \geq 1 \times 10^4$ . Similar to the stationary disturbances, this peak shifts to higher  $\beta$  with increasing Reynolds number. For the larger  $Re_{\delta^*}$  cases in which an appreciable logarithmic overlap layer can be said to occur, the modes associated with this peak have their principal support within the logarithmic region of the mean flow. The increase in spanwise wavenumber is explained by the same reasoning as for the stationary disturbances. As  $Re_{\delta^*}$  increases, the centre of the log region moves closer to the wall in outer-scaled units. For  $y \propto \lambda_z$ , this requires smaller spanwise structures and hence larger spanwise wavenumber. Conversely, the modes associated with the higher  $\omega$  peak at constant  $\beta\delta \approx 2.2$  are centred in the wake region of the mean flow with constant scaling in outer units. Based on this scaling, and the relative location of the corresponding mode shapes within the boundary layer, we refer to these identified modes as log and wake modes, respectively.

Interestingly, the relative amplification of the two peaks changes with increasing  $Re_{\delta^*}$ . In figure 8(a,b), the higher frequency wake modes achieve the highest overall energy amplification. However, as shown in figure 8(c), for  $Re_{\delta^*} \geq 4 \times 10^4$  the lower frequency log modes are most amplified. In both cases the amplification increases with  $Re_{\delta^*}$ , although clearly at different rates. The amplification of the outer-scaled peak initially increases before approximately saturating for higher  $Re_{\delta^*}$ . For  $Re_{\delta^*} \geq 1 \times 10^4$  in which the log peak is distinguishable, the amplification increases approximately as  $Re_{\delta^*}^{0.75}$ . As such, the log modes becomes increasingly dominant as Reynolds number increases.

#### 4.2. Identification of large-scale energetic propagating modes

The spectra in figure 8 identify propagating modes which amplify by several orders of magnitude given optimal forcing by means of an initial condition. However, the pure amplification spectrum is poorly suited to identify scales which, on average, contain the dominant portion of total fluctuating energy. This is better visualized by the premultiplied amplification,  $\beta\omega G_{max}$ , such that equal area corresponds to equal contribution to total integrated kinetic energy on a logarithmic scale. In this case, it is immediately obvious that the stationary modes considered in § 3, and the low frequency modes in figure 8, do not appreciably contribute to total kinetic energy and hence not directly representative of the dominant, energetic motions in turbulent



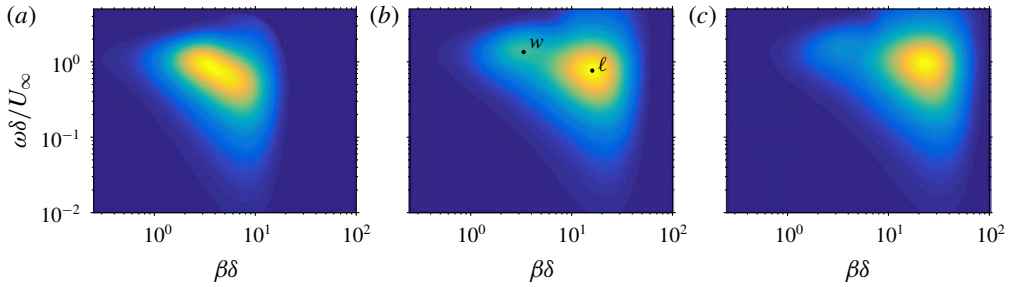


FIGURE 9. (Colour online) Premultiplied amplification,  $\beta\omega G_{max}$ , of the optimal disturbance, (a)  $Re_{\delta^*} = 2 \times 10^3$ , (b)  $Re_{\delta^*} = 2 \times 10^4$ , (c)  $Re_{\delta^*} = 4 \times 10^4$ . In (b), the location of the identified log and wake modes are labelled ‘ $l$ ’ and ‘ $w$ ’, respectively.

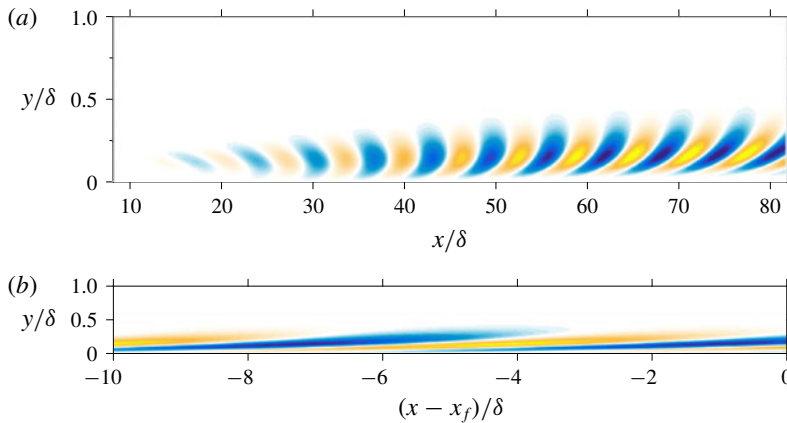


FIGURE 10. (Colour online) Streamwise component of the optimal disturbance response corresponding to the global peak in premultiplied energy amplification at  $Re_{\delta^*} = 2 \times 10^4$  (see figure 9b). (a) Spatial evolution over the full streamwise domain and (b) plotted with equal axis scaling on a shortened streamwise domain. Here,  $\beta\delta = 16.5$  ( $\lambda_z \approx 0.4\delta$ ),  $\omega\delta/U_\infty = 0.76$  ( $\lambda_t = 2\pi/\omega \approx 8.3\delta/U_\infty$ ). At the output, the induced streamwise wavelength is  $\lambda_x \approx 6.1\delta$  with phase velocity  $c \approx 0.74U_\infty$ .

boundary layers. The peaks in figure 8 may, however, be more representative of structures visualized in instantaneous snapshots.

The premultiplied spectra, for the same cases as figure 8, are shown in figure 9. Aside from the absence of low frequency content (note the lower axis limits in figure 9 are different than in figure 8), the premultiplied spectra show similar features. Again at the lowest  $Re_{\delta^*}$  considered, there is insufficient scale separation such that only one elongated peak region is observed. For high  $Re_{\delta^*}$ , two regions are identified associated with the log and wake modes. These are respectively labelled as ‘ $l$ ’ and ‘ $w$ ’ in figure 9. Note the weighting of the premultiplication shifts the locations of these regions to higher spanwise wavenumbers and frequencies as compared to figure 8. Furthermore, for the higher  $Re_{\delta^*}$  the log modes increasingly contain the dominant portion of fluctuation energy content. The scaling of the log and wake modes with increasing Reynolds numbers are discussed in the following section.

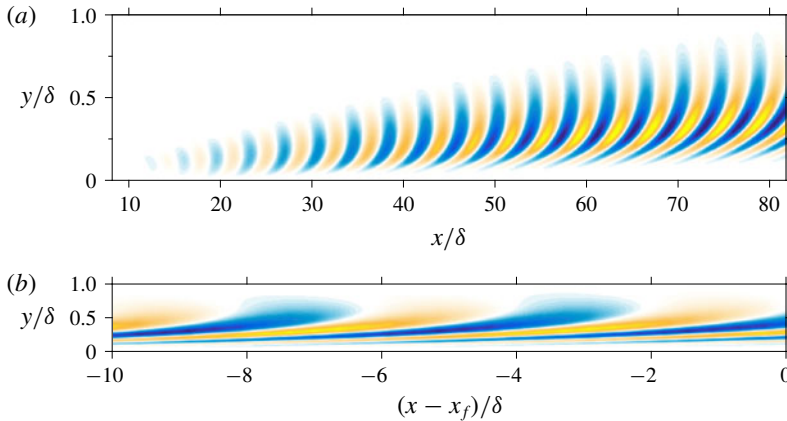


FIGURE 11. (Colour online) Streamwise component of the optimal disturbance response corresponding to the secondary peak in premultiplied energy amplification at  $Re_{\delta^*} = 2 \times 10^4$  (see figure 9*b*). (a) Spatial evolution over the full streamwise domain and (b) plotted with equal axis scaling on a shortened streamwise domain. Here,  $\beta\delta = 3.35$  ( $\lambda_z \approx 1.8\delta$ ),  $\omega\delta/U_\infty = 1.38$  ( $\lambda_t \approx 4.5\delta/U_\infty$ ). At the output, the induced streamwise wavelength is  $\lambda_x \approx 3.7\delta$  with phase velocity  $c \approx 0.82U_\infty$ .

The two classes of structures identified by the peaks in figure 9 are visualized for  $Re_{\delta^*} = 2 \times 10^4$  in figures 10 and 11. Note the location of these modes in the premultiplied energy spectrum are those labelled as  $\ell$  and  $w$  in figure 9*b*). The real component of the optimal streamwise velocity response, given by (2.4), is plotted for arbitrary time and spanwise plane. In figure 10*a*), the log mode is shown over the entire streamwise domain and again in figure 10*b*) for a shortened streamwise domain such that the mode may be visualized with equal axes scaling. The response indicates a wave packet structure attaining its maximum amplitude at the prescribed output plane. As shown in figure 10, the streamwise velocity structures are initially tilted backwards during the early amplification phase and rotate forwards over the streamwise domain as a result of the wall-normal shear. This suggests the Orr mechanism plays a significant role in the early amplification process of these propagating modes, in addition to the optimal alignment of the disturbance phase velocity with that of the local mean. Note the maximum streamwise velocity occurs for  $y < 0.2\delta$ , such that these ‘log modes’ are dominant throughout the log region of the mean flow. Figure 10*b*) provides a more realistic picture of the relative streamwise and wall-normal scales, reminiscent of the streamwise velocity streaks reported in turbulent boundary layers. The wavelength corresponds to  $\lambda_x \approx 6.1\delta$ , in close agreement with the experimentally observed structures and the outer peak in streamwise velocity spectra (Mathis *et al.* 2009).

Similarly, the streamwise velocity response mode corresponding to the secondary wake mode in figure 9*b*) is shown in figure 11. It is immediately recognized that these have a shorter streamwise wavelength than the log modes, with much larger wall-normal extent. They also have significantly less initial upstream tilt, indicating possible reasons why they experience lower amplification than the corresponding log modes (in addition to being centred in a region with less mean shear). As noted in previous discussion, as the wake mode develops in the streamwise direction, it becomes essentially detached from the wall with little to no support in the near

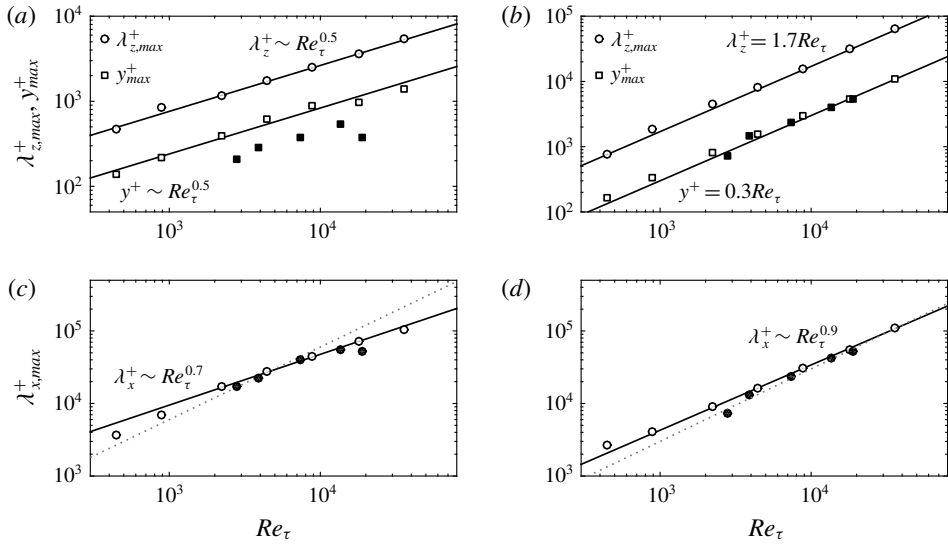


FIGURE 12.  $Re$  scaling of the most energetic optimal disturbance wavelengths, determined from the peaks in pre-multiplied energy amplification (see figure 9). (a,c) Peaks corresponding to log-layer modes, (b,d) the peaks corresponding to wake modes. Open symbols represent data from the current model, filled symbols are experimental data estimated from the pre-multiplied streamwise energy spectra in Mathis *et al.* (2009) for zero-pressure-gradient turbulent boundary layers. The solid lines represent trend lines. In (c), the dotted line corresponds to  $\lambda_x^+ = 6Re_\tau$  in accordance with the generally accepted scaling of the streamwise wavenumber. In (d) the dotted line corresponds to  $\lambda_x^+ = 3Re_\tau$ .

wall region. The dominant contribution comes in the wake of the mean flow, well outside the log layer, with the ‘heads’ protruding near the edge of the boundary layer (figure 11b).

#### 4.3. Scaling of the propagating modes and comparison with experimental measurements

Here we present the  $Re$ -scaling of the most energetic optimal disturbance modes and a comparison to energetic scales observed in turbulent boundary layers. To this end, we extract length scales associated with the log and wake mode peaks in the pre-multiplied amplification spectra (see figure 9), denoted with the subscript ‘max’, for  $Re_{\delta^*} = 2 \times 10^3 - 1.6 \times 10^5$ , or  $Re_\tau \approx 446 - 36\,000$ . These results are plotted in wall units as a function of  $Re_\tau$  in figure 12(a,c) for the log modes and 12(b,d) for the wake modes. We also plot experimental data, estimated from the pre-multiplied streamwise energy spectra of Mathis *et al.* (2009) for high  $Re$  turbulent boundary layers. In this case, the location of the ‘outer peak’ in the streamwise energy spectra generally associated with ‘superstructures’ (or VLSMs), is plotted alongside the log modes. Similarly, the approximate location of the emergence of the ‘outer hump’, as described by Monty *et al.* (2009) and associated with the LSMs, is plotted alongside the wake modes. Note that no matching information is available for the spanwise wavelengths.

Figure 12(a) shows the extracted spanwise and wall-normal scaling the log modes. Similar to the stationary modes in figure 4(b), both the inner-scaled spanwise

wavelength and wall-normal position vary approximately as  $Re_\tau^{0.5}$  for the  $Re$  range considered here. Following the discussion in § 3.1, this  $Re_\tau$ -dependence is in agreement with the scaling of the geometric centre of the logarithmic layer of the mean flow, and the approximate location of the peak Reynolds shear stress (Sreenivasan 1989). The wall-normal position of the optimal disturbance energy lies slightly above the location of the outer peak in the experimental measurements. However, the approximate square root scaling is well predicted. The aspect ratio of the log modes remains approximately constant in the streamwise plane, with spanwise wavelength given by  $\lambda_{z,max}^+ \approx 26Re_\tau^{1/2}$ . As a practical consideration, note the increase in both  $y_{max}^+$  and  $\lambda_{z,max}^+$  expressed in wall units is associated with a corresponding decrease in outer units as  $Re_\tau^{-1/2}$  (i.e. if  $y^+ \sim Re_\tau^p \implies y/\delta \sim Re_\tau^{p-1}$  for arbitrary power,  $p$ ). This requires the energetic modes move closer to the wall relative to local boundary layer thickness with decreasing spanwise wavelength as  $Re$  increases.

The streamwise wavelength of the log mode displays different scaling than the wall-normal and spanwise scales, as shown in figure 12(c). A simple linear regression analysis on the logarithmic-scaled data yields  $\lambda_{x,max}^+ \sim Re_\tau^{0.7}$ , indicating a Reynolds number dependence and hence slight shortening in streamwise length relative to the boundary layer thickness. Note the two lower  $Re_\tau$  points have not been included in the fit as there is no clear distinction between the log and wake modes (see figure 9a). It is generally accepted the outer peak in premultiplied streamwise energy spectra is approximately fixed in outer units with  $\lambda_x \approx 6\delta$  (Hutchins & Marusic 2007a). This requires the inner-scaled wavelength increase linearly as  $\lambda_x^+ \approx 6Re_\tau$  (dotted line in figure 12c). However, recent high Reynolds number experimental data indicate a  $Re_\tau^{0.5}$  dependence on the streamwise wavelength associated with the outer peak (Vallikivi, Ganapathisubramani & Smits 2015). This is in agreement with the present results in that there may be at least a moderate Reynolds number dependence. Nevertheless, the agreement in figure 12(c) between the computed streamwise wavelengths of the optimal disturbance log modes and the outer peak in the experimental measurements over roughly an order of magnitude in  $Re_\tau$  is encouraging. Both the best fit and a  $6Re_\tau$  trend line are shown for comparison.

In figure 12(b,d), we show the respective scaling of the wake modes and comparison of the approximated LSMs in Mathis *et al.* (2009). Again, both the spanwise and wall-normal scales of the optimal disturbance modes scale similarly. However, here they show approximately linear increase with  $Re_\tau$ , or constant scaling in terms of boundary layer heights. In this case,  $y \approx 0.3\delta$  with  $\lambda_z \approx 1.7\delta$ . Note, consistent with this outer scaling, these modes are centred in the wake region of the mean flow, with diminishing support extending towards the wall (e.g. figure 11). The associated streamwise wavelength, plotted in figure 12(d), reveals a weak  $Re_\tau$ -dependence with  $\lambda_x^+ \sim Re_\tau^{0.9}$ . Similar to the streamwise scales of the log modes, this indicates a slight shortening of  $\lambda_x/\delta$  with increasing Reynolds number. Over the range of  $Re_\tau$  considered here,  $\lambda_x \approx 3\text{--}4\delta$ , in good agreement with the location of the outer hump in the streamwise energy spectra (Monty *et al.* 2009). The dotted line in figure 12(d) denotes  $\lambda_x = 3\delta$ .

## 5. Summary and discussion

Optimal disturbances have been computed in a turbulent boundary layer in which the spatial development of the mean flow is retained through a parabolized formulation. The classical spatial approach for steady disturbances is modified to also consider travelling wave disturbances where the local streamwise wavenumber is computed as

part of the optimization algorithm. In the context of disturbances developing about a turbulent mean flow, optimal disturbances are viewed as the homogeneous solution to the equations governing the fluctuations subject to a turbulent forcing at particular wavenumber/frequency combinations. The main findings from the present study are summarized here.

We find both steady and travelling wave modes achieve energy amplification up to several orders of magnitude. All identified modes correspond to streaky structures, with streamwise length scales larger than their corresponding spanwise scales. The computed amplification and optimal scales show a strong dependence on the local mean flow and the streamwise development length, or separation between input and output planes. In particular, as shown for steady disturbances, the largest and most amplified disturbances are generated farthest upstream. As the separation between input/output planes is reduced, there is a monotonic decrease in peak amplification and associated spanwise wavelength. For steady disturbances, a single peak is identified in the amplification spectra as a function of spanwise wavenumber. Disturbances associated with this peak attain their maximum velocity near the centre of the logarithmic layer of the mean flow. As such, the spanwise wavelength and wall-normal position, in inner-scaled units, increases as  $\sim Re_\tau^{0.5}$ . In addition, the premultiplied streamwise energy spectra reveal a second, dominant peak in constant inner-scaled units with spanwise and wall-normal scaling similar to the near wall streaks.

For all Reynolds numbers and parameter combinations considered, travelling wave optimal disturbances achieve significantly higher energy amplification than steady disturbances. These disturbances have convection velocities approximately equal to the local mean flow, related to critical layer behaviour. For high Reynolds numbers, in which a sufficient separation of outer and inner scales occurs, two peaks are identified in the amplification spectra for propagating modes. Both of these peaks occur for different spanwise wavenumber than the steady disturbances. An outer-scaled peak, with approximately constant spanwise wavelength in terms of boundary layer height, dominates for low to moderately high Reynolds numbers. A mixed-scaling peak, which shifts to smaller spanwise wavelength in terms of boundary layer height for increasing Reynolds numbers, dominates at the highest Reynolds numbers investigated.

The premultiplied amplification spectra is used to identify scales which contribute most to total fluctuation energy. Similar to the pure amplification spectra, two classes of modes are identified. These are referred to as log and wake modes based on their identified scaling and location within the boundary layer mean flow profile. The wake modes have their principal support in the wake of the turbulent mean flow, essentially detached from the wall, with peak velocity at  $y \approx 0.3\delta$ , spanwise wavelength  $\lambda_z \approx 1.7\delta$  and convection velocity  $c \approx 0.82U_\infty$ . The streamwise wavelength shows a slight Reynolds number dependence, with  $\lambda_x \approx 3-4\delta$  over approximately two orders of magnitude in Reynolds number. For moderately high Reynolds numbers, the log modes increasingly dominate the contribution to fluctuating energy. The wall-normal and spanwise scaling of the log modes is similar to the steady disturbances, with the inner-scaled wall-normal position and spanwise wavelength increasing as  $\sim Re_\tau^{0.5}$ . The streamwise wavelength shows moderate Reynolds number dependence, increasing in inner-scaled units as  $\sim Re_\tau^{0.7}$ . Over the range of Reynolds numbers considered,  $\lambda_x$  ranges from  $4-8\delta$  with convection velocity  $c \approx 0.74U_\infty$ . The identified energetic scales are shown to be in good quantitative agreement with established energetic motions in natural turbulent boundary layers.

### 5.1. Comparison of results with related gain-based approaches

The current approach is related to several recent studies on the linear amplification properties of the Navier–Stokes equations about wall-bounded flows. In particular, Cossu *et al.* (2009) has studied temporal optimal disturbances with the same mean flow profile used here along with a parallel flow approximation. An eddy viscosity was also included to model the interaction of incoherent background turbulence with the amplified disturbances. Qualitatively, the optimization results in Cossu *et al.* (2009) are similar to the (steady) disturbances presented here in that streaky structures are amplified with spanwise and wall-normal velocity components generating large streamwise velocity response. Quantitative results are quite different, however. Cossu *et al.* (2009) identified two peaks in the amplification spectrum, one corresponding to very large disturbances ( $\lambda_z \approx 8\delta$ ) centred at the edge of the boundary layer and one inner-scaled peak associated with buffer layer structures with scaling similar to near wall streaks ( $\lambda_z^+ \approx 81$ ). Negligible amplification was found for structures within the logarithmic region of the mean flow. As such, aside from the inner layer structures identified here in the streamwise energy density, the most amplified disturbances are orders of magnitude different in spanwise wavelength and wall-normal position with the steady optimal disturbances identified in the current results. A potential reason for such discrepancy is the use of the eddy viscosity in Cossu *et al.* (2009) (see also § 5.3). However, using only the molecular viscosity in the temporal optimal disturbance results does not appear to improve the agreement. Note the temporal optimal disturbances may be regarded as fundamentally different than the current spatial implementation, because those disturbances are neither steady nor time harmonic propagating modes as in the current approach.

Recently, Hack & Moin (2017) have examined propagating optimal disturbances in spatially developing laminar boundary layers within the PSE framework. In contrast to current approach, Hack & Moin (2017) do not employ an adjoint-based solver but rather use an expansion based on local, parallel eigenfunctions coupled with their downstream evolution via the PSE linear operator. As such, Hack & Moin (2017) do not evolve the converged optimal disturbance with a single (spatially evolving) streamwise wavenumber. Rather, each spatially evolving eigenfunction develops according to the streamwise wavenumber selected by the PSE auxiliary equation. In the current method, the conventional PSE auxiliary equation is not used. Although the formulation and base flow differ (laminar versus turbulent), Hack & Moin (2017) also find the largest energy amplification with three-dimensional disturbances of finite frequency resulting from the interaction of the Orr and lift-up mechanisms.

An approach more closely related to the current formulation is the resolvent analysis of Moarref *et al.* (2013), although performed for parallel turbulent channel flow. The resolvent approach identifies both steady and propagating modes and the current method degenerates to the same linear operator if the streamwise derivative of the disturbance is neglected. Moarref *et al.* (2013) focused on energetic scales based on the rank 1 model of streamwise energy density. Two classes of large scale structures were identified: an outer and so-called middle peak corresponding essentially to the wake and log modes identified here. The wall-normal and spanwise scales of the middle peak are in good quantitative agreement with the present results. The streamwise wavelengths identified here are shorter (i.e.  $\lambda_x \approx 6\delta$  as opposed to  $\lambda_x \approx 12\text{--}16h$ ). However, these are consistent with differences observed experimentally between internal (channel) and external (boundary layer) flows (Monty *et al.* 2009). The largest difference is seen with regard to the outer peak, or wake modes. The identified wall-normal and spanwise scales are similar,  $y \approx 0.45h$  and



$\lambda_z \approx 2h$  in Moarref *et al.* (2013) as compared to  $y \approx 0.3\delta$  and  $\lambda_z \approx 1.7\delta$  here. Again, these are consistent with experimentally observed trends. However, in Moarref *et al.* (2013), the streamwise scales of the outer peak increased as  $\lambda_x/h \sim 0.1Re_\tau$  indicating an increase in the outer-scaled wavelength with increasing Reynolds number and structures much larger than observed experimentally. In the current spatial approach, the corresponding structures show a slight decrease in outer-scaled streamwise wavelength with increasing Reynolds number and lengths  $\lambda_x \approx 3-4\delta$ , in good agreement with experimental observations (Monty *et al.* 2009). Furthermore, Moarref *et al.* (2013) showed an increase in the relative strength of the outer peak structures with increasing  $Re_\tau$ . In contrast, here we find the relative amplification of the wake modes decreases with  $Re_\tau$  such that the log modes become increasingly dominant at higher Reynolds numbers. Of course, a comparison is somewhat limited as the mean flows are different. However, it does appear the spatial implementation significantly alters the development of at least the largest energetic scales.

### 5.2. Spatial formulation and influence of the spatial development of the mean flow

In the current formulation, the spatial development enters through both the streamwise evolution of the mean flow and through the streamwise development/lifetime of the disturbance. The disturbances are purely harmonic in time. However, these disturbances are ‘transient’ in the streamwise direction. A small disturbance generated far upstream will have negligible amplitude sufficiently far downstream, regardless of the initial amplification.

In comparing with related analyses under parallel approximations, we may then ask which effect is more critical in determining optimal scales: the evolution of the mean flow, or the transient streamwise development of the disturbance. The latter includes any history effects as well. Of course, perhaps for all but the smallest-scale disturbances, these two effects may be inextricably bound. Nevertheless, the identified scaling in §§ 3 and 4 indicates that the disturbance lifetime and local mean flow are the dominant factors in selecting the preferential scales. In all the results presented in this study, although the disturbance evolves in a spatially varying mean flow, the scaling is presented based on the mean flow scales at the final output plane (i.e. the  $Re_{\delta^*}$  the case has been labelled). This is consistent with typical experimental measurements. Although we observe some scatter in the  $Re$  scaling (e.g. figure 12), which may be expected in particular because the composite mean profile is not self-similar, the identified trends appear to scale quite well using only the mean flow scales at the output. This suggests the optimal scales adjust rather quickly to the local mean flow, despite the fact that the mean flow may be substantially different far upstream where the disturbance was generated (for large scales).

### 5.3. Turbulent mean flow and eddy viscosity

The nonlinear source term involving the fluctuating Reynolds stresses is treated here as a generic internal forcing at particular wavenumber/frequency combinations (McKeon & Sharma 2010; Beneddine *et al.* 2016). This provides a consistent means to study the linear amplification properties of disturbances about a turbulent mean. Note, however, that no explicit distinction is made between the nature of fluctuations in the Reynolds decomposition. Coherent disturbances are rather implied through maximizing kinetic energy and the rank 1 approximation. Alternatively, one may consider a triple decomposition (Reynolds & Hussain 1972) in which the flow is decomposed into a mean, coherent fluctuation, and so-called background turbulent motion. Deriving the

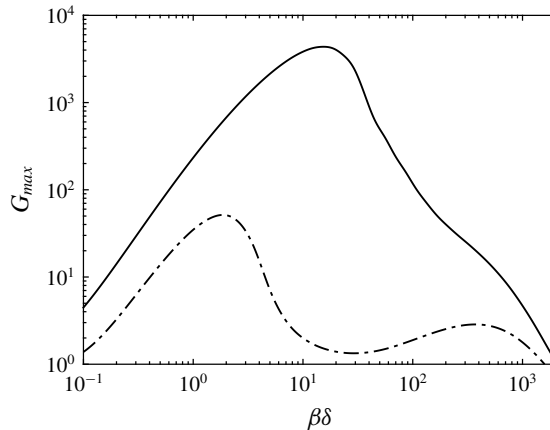


FIGURE 13. Spatial envelope of maximum energy amplification for steady, streamwise elongated disturbances ( $\alpha = \omega = 0$ ), computed for  $Re_{\delta^*} = 2 \times 10^4$ . (—): quasi-laminar, (---): eddy viscosity.

equations for the coherent fluctuations generates Reynolds stresses associated with the fluctuations and background turbulence. Modelling the Reynolds stresses of the background turbulence typically involves introducing an eddy viscosity based on the turbulent mean flow (e.g. Viola *et al.* 2014). Neglecting them is generally referred to as a quasi-laminar approach, equivalent to assuming the background turbulence only effects the development of the coherent motion implicitly through modification of the turbulent mean flow, with the resulting linearized equations equivalent to those used in the current study.

In general, use of an eddy viscosity produces larger structures with significantly less amplification, as previously noted. In figure 13, we briefly compare the results of the current spatial approach with those computed using an eddy viscosity as in Cossu *et al.* (2009) for steady disturbances ( $\omega = 0$ ) at  $Re_{\delta^*} = 2 \times 10^4$ . We refer to the results without the eddy viscosity as quasi-laminar and note these are identical to the results in § 3. Figure 13 shows the disturbances computed using the eddy viscosity have significantly less amplification ( $\sim 2$  orders of magnitude) as a result of the additional large artificial dissipation. Furthermore, the eddy viscosity results reveal the two-peak structure, similar to that identified in del Álamo & Jiménez (2006) and Cossu *et al.* (2009), with a relatively high amplitude outer peak at small  $\beta$  and a low amplitude inner peak at high  $\beta$ . Repeating the calculations at various  $Re$  identifies the outer peak with constant scaling in outer units ( $\lambda_z \approx 3.4\delta$ ) and inner peak with constant scaling in wall units ( $\lambda_z^+ \approx 80$ ). The inner peak agrees well with the inner peak identified by Cossu *et al.* (2009), with nearly identical amplification. The outer peak, however, occurs for much shorter spanwise wavelength (but with similar amplification),  $\lambda_z \approx 3.4\delta$  as compared to  $\lambda_z \approx 8\delta$  in Cossu *et al.* (2009). More importantly, the region between the two peaks in the eddy viscosity results has essentially negligible amplification. Note that this local minimum corresponds to the region for which the quasi-laminar results have maximum amplification. This range of spanwise wavelengths has been associated with structures having peak velocity in the log region of the mean flow (§ 3), known to be dominated by energetic motions in real turbulent boundary layers. The minimum amplification in the eddy viscosity results arise because the Reynolds shear stress peaks near the centre of the log layer

and as such, the eddy viscosity is high. This tends to dampen the growth of optimal disturbances. We cannot expect the eddy viscosity results to predict the energetic log modes in this gain-based approach, without resorting to a secondary instability mechanism (e.g. Alizard (2015)). Indeed, attempting to reconstruct streamwise energy density using the eddy viscosity optimal disturbance modes and amplification, as in (3.1) and shown figure 5 for the quasi-laminar results, yields non-physical results.

#### 5.4. Outlook

The current study is focused on the downstream response to upstream initial conditions/forcing (at a single plane), as in conventional spatial optimal disturbances. This has been formulated as the homogeneous solution to the governing equations subject to a distributed, internal turbulent forcing. While the linearized operator examined here includes all the relevant dynamics, it would be beneficial to examine the full solution and optimal response to distributed forcing. For the boundary layer, the largest scales are most sensitive to upstream forcing. As such, the distributed forcing is likely to have the largest impact on the smallest scales, in which the streamwise location of the forcing amplitude is freely permitted to shift downstream closer to the output optimization plane. In this case, it would be unnecessary to vary the location of the input plane as in §3 provided the full streamwise domain is sufficiently resolved.

Finally, we have shown that the most energetic optimal disturbances, arising from simple, linear analysis, shows good agreement with energetic motions naturally observed in turbulent boundary layers. In particular, this is especially the case for propagating modes considered with scales resembling LSMs and VLSMs. This supports the view that these structures may be essential, fundamental elements to wall turbulence (Sharma & McKeon 2013). Of course, real turbulent motions are not optimized or linear. As the amplification presented here is computed as the response to unit forcing across all frequencies and wavenumbers, quantitative differences may be expected between the predicted optimal scales and the structures observed in natural turbulent boundary layers. This analysis examines the optimized response to forcing, but makes no attempt at describing how or if a particular forcing may occur in real turbulent flows. However, we would expect a large response if the boundary layer is artificially forced at the most amplified wavenumbers/frequencies. As such, the present results may also serve to guide potential passive and active control schemes, in particular when a finite streamwise domain is considered.

#### Acknowledgements

This work was partially supported by grants from the National Science Foundation (award no. 1510919), Air Force Office of Scientific Research (award no. FA9550-14-1-0167), Army Research Office (award no. W911NF-13-1-0115) and the Florida Center for Advanced Aero-Propulsion.

#### Appendix A. Governing equations and discretization

The parabolized equations governing the amplitude function  $\hat{q}$  subject to forcing  $\hat{f}$  are given by (2.10),

$$\mathbf{A}\hat{q} + \mathbf{B}\frac{\partial\hat{q}}{\partial x} + \mathbf{C}\frac{\partial\hat{q}}{\partial y} + \mathbf{D}\frac{\partial^2\hat{q}}{\partial y^2} = \mathbf{E}\hat{f}, \quad (\text{A } 1)$$

where the coefficient matrices **A**, **B**, **C**, **D**, **E** are given by

$$\mathbf{A} = \begin{pmatrix} a + \partial_x \bar{u} & \partial_y \bar{u} & 0 & i\alpha \\ \partial_x \bar{v} & a + \partial_y \bar{v} & 0 & 0 \\ 0 & 0 & a & i\beta \\ i\alpha & 0 & i\beta & 0 \end{pmatrix}, \quad \mathbf{B} = \begin{pmatrix} \bar{u} & 0 & 0 & 1 \\ 0 & \bar{u} & 0 & 0 \\ 0 & 0 & \bar{u} & 0 \\ 1 & 0 & 0 & 0 \end{pmatrix}, \quad (\text{A } 2a,b)$$

$$\mathbf{C} = \begin{pmatrix} \bar{v} & 0 & 0 & 0 \\ 0 & \bar{v} & 0 & 1 \\ 0 & 0 & \bar{v} & 0 \\ 0 & 1 & 0 & 0 \end{pmatrix}, \quad \mathbf{D} = -\frac{1}{Re} \begin{pmatrix} 1 & 0 & 0 & 0 \\ 0 & 1 & 0 & 0 \\ 0 & 0 & 1 & 0 \\ 0 & 0 & 0 & 0 \end{pmatrix}, \quad \mathbf{E} = \begin{pmatrix} 1 & 0 & 0 & 0 \\ 0 & 1 & 0 & 0 \\ 0 & 0 & 1 & 0 \\ 0 & 0 & 0 & 0 \end{pmatrix}, \quad (\text{A } 3a-c)$$

with

$$a = i(\alpha \bar{u} - \omega) + \frac{1}{Re}(\alpha^2 + \beta^2). \quad (\text{A } 4)$$

Note the  $b_{14}$  term in the matrix **B** corresponds to the streamwise derivative of the pressure amplitude function and may be neglected (in particular, to eliminate residual ellipticity in the equations).

In (A 1), the wall-normal direction is discretized using a spectral collocation method based on Chebyshev polynomials. The Chebyshev collocation points,  $\xi \in [-1, 1]$ , are mapped to the physical domain,  $y \in [0, y_{max}]$ , using the rational mapping (Hanifi *et al.* 1996),

$$y = \hat{a} \frac{1 + \xi}{\hat{b} - \xi} \quad (\text{A } 5)$$

with

$$\hat{a} = \frac{y_c y_{max}}{y_{max} - 2y_c}, \quad \hat{b} = 1 + \frac{2\hat{a}}{y_{max}}. \quad (\text{A } 6a,b)$$

This mapping clusters the collocation points near the wall to capture the steep gradients in both the turbulent mean flow and solution  $\hat{q}$ . The parameters  $\hat{a}$  and  $\hat{b}$  control the point distribution, with half the collocation points mapped to the interval  $[0, y_c]$ . To resolve the energetic, log-layer structures,  $y_c$  is chosen near the centre of the logarithmic region of the mean flow, estimated as  $y_c^+ = 4.5 Re_\tau^{1/2}$  with  $Re_\tau = \delta u_\tau / \nu$  the friction Reynolds number and  $+$  denoting inner units. This ensures that, with increasing Reynolds number, the most energetic structures are well resolved.

The streamwise direction in (A 1) discretized into  $N_x$  points  $x_j = x_0 + j\Delta x_j$  for  $j = 0, \dots, N_x - 1$  and  $\Delta x_j = x_j - x_{j-1}$ . In this study, we take  $\Delta x_j = \Delta x$ , such that the streamwise derivative at  $x_j$  may be approximated using the second-order backwards difference

$$\frac{\partial \hat{q}}{\partial x} \approx \frac{3\hat{q}_j - 4\hat{q}_{j-1} + \hat{q}_{j-2}}{2\Delta x}. \quad (\text{A } 7)$$

On the first plane,  $j = 1$ , the first-order backwards difference is used. Substitution of (A 7) into (A 1) (with  $\hat{f} = 0$ ) yields the linear system

$$\mathbf{A}_j \hat{q}_j = \mathbf{B}_j \hat{q}_{j-1} + \mathbf{C}_j \hat{q}_{j-2} \quad (\text{A } 8)$$

to be solved at each streamwise plane  $x_j$  for the amplitude functions  $\hat{q}_j$ .

**Appendix B. Adjoint equations and the optimality system**

Here we present an abridged derivation of the optimality system and adjoint equations using the method of Lagrange multipliers. Rather than writing the optimal disturbance as in §2.4 in terms of the state-transition matrix  $\Phi_u$ , we formulate the equivalent constrained optimization problem in which the goal is to maximize a specified objective function(al) subject to additional constraints. In this case, the objective function is the amplification from an initial condition at  $x_0$  to the corresponding response at  $x_f$ , subject to the state equation (2.10). As such, we define

$$\mathcal{J}(\hat{q}) = \frac{\|\hat{u}(x_f)\|^2}{\|\hat{u}(x_0)\|^2} = \int_0^\infty \hat{u}^H \hat{u}|_{x_f} dy \tag{B 1}$$

as the objective function where it is assumed that the initial condition has been scaled to unit energy norm, and only the velocity components are considered. It is required that  $\hat{q}$  satisfy (2.10), namely

$$F(\hat{q}) = \mathbf{A}\hat{q} + \mathbf{B}\frac{\partial \hat{q}}{\partial x} + \mathbf{C}\frac{\partial \hat{q}}{\partial y} + \mathbf{D}\frac{\partial^2 \hat{q}}{\partial y^2} - \mathbf{E}\hat{f} = 0. \tag{B 2}$$

We may then define the Lagrange function as the augmented objective function

$$\mathcal{L}(\hat{q}, \hat{q}^+) = \mathcal{J}(\hat{q}) - \langle \hat{q}^+, F(\hat{q}) \rangle, \tag{B 3}$$

where the second term is associated with the scalar product defined over the entire domain,

$$\langle \hat{q}^+, F(\hat{q}) \rangle = \int_{x_0}^{x_f} \int_0^\infty \hat{q}^{+H} F(\hat{q}) dy dx. \tag{B 4}$$

Here,  $\hat{q}^+ = (\hat{u}^+, \hat{v}^+, \hat{w}^+, \hat{p}^+)^T$  is referred to as the Lagrange multiplier, or adjoint state. Formally, we could introduce additional Lagrange multipliers in (B 3) to enforce the initial condition to (A 1) at  $x_0$  and to enforce the scaling to unit norm. These are neglected for compactness. A necessary condition for optimality of (B 3) is that first order variations in the Lagrangian  $\delta\mathcal{L}$  subject to variations in the states  $\delta\hat{q}$  and  $\delta\hat{q}^+$  are zero, i.e.

$$\frac{\delta\mathcal{L}}{\delta\hat{q}^+} = \lim_{\varepsilon \rightarrow 0} \frac{\mathcal{L}(\hat{q}, \hat{q}^+ + \varepsilon\tilde{q}^+) - \mathcal{L}(\hat{q}, \hat{q}^+)}{\varepsilon} = 0, \quad \forall \tilde{q}^+ \tag{B 5}$$

and similarly for  $\delta\mathcal{L}/\delta\hat{q}$ . Evaluation of (B 5), and requiring that this vanish for all arbitrary  $\tilde{q}^+$ , retrieves the original constraint equation  $F(\hat{q}) = 0$ . Similarly, evaluating  $\delta\mathcal{L}/\delta\hat{q}$ , we obtain (after applying integration by parts)

$$\begin{aligned} \frac{\delta\mathcal{L}}{\delta\hat{q}} &= 2 \int_0^\infty \hat{u}^H \tilde{u}|_{x_f} dy - \int_{x_0}^{x_f} \int_0^\infty \left[ \left( \hat{q}^{+H} \mathbf{A} - \frac{\partial \hat{q}^{+H}}{\partial x} \mathbf{B} - \frac{\partial \hat{q}^{+H}}{\partial y} \mathbf{C} + \frac{\partial^2 \hat{q}^{+H}}{\partial y^2} \mathbf{D} \right) \tilde{q} \right. \\ &\quad \left. + \hat{q}^{+H} \left( \frac{\partial \mathbf{B}}{\partial x} + \frac{\partial \mathbf{C}}{\partial y} \right) \tilde{q} \right] dy dx - \int_0^\infty \left[ \hat{q}^{+H} \mathbf{B} \tilde{q} \right]_{x_0}^{x_f} dy \\ &\quad - \int_{x_0}^{x_f} \left[ \hat{q}^{+H} \mathbf{C} \tilde{q} + \hat{q}^{+H} \mathbf{D} \frac{\partial \tilde{q}}{\partial y} - \frac{\partial \hat{q}^{+H}}{\partial y} \mathbf{D} \tilde{q} \right]_0^\infty dx. \end{aligned} \tag{B 6}$$

The first term arises from the objective function (B 1) and the remaining terms derive from the scalar product (B 4). The term  $\partial_x \mathbf{B} + \partial_y \mathbf{C}$  is zero as the mean flow satisfies continuity. In order for (B 6) to vanish for all arbitrary variations  $\tilde{\mathbf{q}}$ , we require the adjoint state  $\hat{\mathbf{q}}^+$  to satisfy

$$\mathbf{A}^H \hat{\mathbf{q}}^+ - \mathbf{B}^H \frac{\partial \hat{\mathbf{q}}^+}{\partial x} - \mathbf{C}^H \frac{\partial \hat{\mathbf{q}}^+}{\partial y} + \mathbf{D}^H \frac{\partial^2 \hat{\mathbf{q}}^+}{\partial y^2} = 0. \quad (\text{B } 7)$$

Equation (B 7) is the adjoint equation to (A 1). Note the adjoint equation has a similar form to the forward equation, with the sign of first derivative terms appearing negative due to the integration by parts. As such, equation (B 7) is integrated backwards in space, from  $x_0$  to  $x_f$ . Initial and boundary conditions for (B 7) are derived by requiring the remaining boundary terms in (B 6) are zero for arbitrary  $\tilde{\mathbf{q}}$ . Expanding the last term in (B 6), and after simplification, we choose boundary conditions to match the forward equations,

$$y = 0 : \hat{u}^+ = \hat{v}^+ = \hat{w}^+ = 0 \quad (\text{B } 8)$$

$$y \rightarrow \infty : \hat{u}^+ = \hat{w}^+ = \hat{p}^+ = 0. \quad (\text{B } 9)$$

Similarly, the initial conditions to the adjoint equation at  $x_f$  are given by

$$\bar{u}\hat{u}^+ + \hat{p}^+ = \hat{u} \quad (\text{B } 10)$$

$$\bar{u}\hat{v}^+ = \hat{v} \quad (\text{B } 11)$$

$$\bar{u}\hat{w}^+ = \hat{w}. \quad (\text{B } 12)$$

Here, it has been assumed the term in  $\mathbf{B}$  associated with the streamwise pressure gradient has been neglected. The terminal conditions of (B 6) at  $x_0$  are assigned to the initial condition of the forward equation to achieve the optimality conditions. This arises naturally in (B 6) if it were not assumed in (B 1) that  $\|\hat{\mathbf{u}}(x_0)\|^2 = 1$ . The initial conditions for  $\hat{\mathbf{q}}$  at  $x_0$  are then given by

$$\hat{u} = \bar{u}\hat{u}^+ + \hat{p}^+ \quad (\text{B } 13)$$

$$\hat{v} = \bar{u}\hat{v}^+ \quad (\text{B } 14)$$

$$\hat{w} = \bar{u}\hat{w}^+. \quad (\text{B } 15)$$

As in Tempelmann *et al.* (2010), we neglect the adjoint pressure  $\hat{p}^+$  in the initial condition (B 10). In the upstream marching solution of (B 7), we use a second-order forwards difference for the discretization of the streamwise derivative. The wall-normal discretization is the same as the forward solution.

## REFERENCES

- ADRIAN, R. J. 2007 Hairpin vortex organization in wall turbulence. *Phys. Fluids* **19** (4), 041301.
- ADRIAN, R. J., MEINHART, C. D. & TOMKINS, C. D. 2000 Vortex organization in the outer region of the turbulent boundary layer. *J. Fluid Mech.* **422**, 1–54.
- DEL ÁLAMO, J. C. & JIMÉNEZ, J. 2006 Linear energy amplification in turbulent channels. *J. Fluid Mech.* **559**, 205–213.
- ALIZARD, F. 2015 Linear stability of optimal streaks in the log-layer of turbulent channel flows. *Phys. Fluids* **27** (10), 105103.



- ANDERSSON, P., BERGGREN, M. & HENNINGSIN, D. 1999 Optimal disturbances and bypass transition in boundary layers. *Phys. Fluids* **11**, 134–150.
- BALAKUMAR, B. J. & ADRIAN, R. J. 2007 Large- and very-large-scale motions in channel and boundary-layer flows. *Phil. Trans. R. Soc. A* **365** (1852), 665–681.
- BENEDDINE, S., SIPP, D., ARNAULT, A., DANDOIS, J. & LESSHAFFT, L. 2016 Conditions for validity of mean flow stability analysis. *J. Fluid Mech.* **798**, 485–504.
- BUTLER, K. & FARRELL, B. 1993 Optimal perturbations and streak spacing in wall-bounded turbulent shear flow. *Phys. Fluids* **5**, 774–777.
- BUTLER, K. M. & FARRELL, B. 1992 Three-dimensional optimal perturbations in viscous shear flow. *Phys. Fluids A* **4** (8), 1637–1650.
- COSSU, C., PUJALS, G. & DEPARDON, S. 2009 Optimal transient growth and very large-scale structures in turbulent boundary layers. *J. Fluid Mech.* **619**, 79–94.
- DENNIS, D. & NICKELS, T. 2011a Experimental measurement of large-scale three-dimensional structures in a turbulent boundary layer. Part 1. Vortex packets. *J. Fluid Mech.* **673**, 180–217.
- DENNIS, D. & NICKELS, T. 2011b Experimental measurement of large-scale three-dimensional structures in a turbulent boundary layer. Part 2. Long structures. *J. Fluid Mech.* **673**, 218–244.
- EITEL-AMOR, G., ÖRLÜ, R. & SCHLATTER, P. 2014 Simulation and validation of a spatially evolving turbulent boundary layer up to  $Re_\theta = 8300$ . *Intl J. Heat Fluid Flow* **47** (C), 57–69.
- EITEL-AMOR, G., ORLU, R., SCHLATTER, P. & FLORES, O. 2015 Hairpin vortices in turbulent boundary layers. *Phys. Fluids* **27** (2), 025108.
- ELLINGSEN, T. & PALM, E. 1975 Stability of linear flow. *Phys. Fluids* **18** (4), 487–488.
- FARRELL, B. F. & IOANNOU, P. J. 1996 Generalized stability theory. Part II. Nonautonomous operators. *J. Atmos. Sci.* **53** (14), 2041–2053.
- GUSTAVSSON, L. H. 1991 Energy growth of three-dimensional disturbances in plane poiseuille flow. *J. Fluid Mech.* **224**, 241–260.
- HACK, M. J. P. & MOIN, P. 2017 Algebraic disturbance growth by interaction of Orr and lift-up mechanisms. *J. Fluid Mech.* **829**, 112–126.
- HANIFI, A., SCHMID, P. & HENNINGSON, D. 1996 Transient growth in compressible boundary layer flow. *Phys. Fluids* **8** (3), 826–833.
- HEAD, M. R. & BANDYOPADHYAY, P. 1981 New aspects of turbulent boundary-layer structure. *J. Fluid Mech.* **107**, 297–338.
- HERBERT, T. 1997 Parabolized stability equations. *Annu. Rev. Fluid Mech.* **29** (1), 245–283.
- HUTCHINS, N., HAMBLETON, W. T. & MARUSIC, I. 2005 Inclined cross-stream stereo particle image velocimetry measurements in turbulent boundary layers. *J. Fluid Mech.* **541**, 21–54.
- HUTCHINS, N. & MARUSIC, I. 2007a Evidence of very long meandering features in the logarithmic region of turbulent boundary layers. *J. Fluid Mech.* **579**, 1–28.
- HUTCHINS, N. & MARUSIC, I. 2007b Large-scale influences in near-wall turbulence. *Phil. Trans. R. Soc. Lond. A* **365** (1852), 647–664.
- HWANG, Y. & COSSU, C. 2010 Linear non-normal energy amplification of harmonic and stochastic forcing in the turbulent channel flow. *J. Fluid Mech.* **664**, 51–73.
- JIMÉNEZ, J. & PINELLI, A. 1999 The autonomous cycle of near-wall turbulence. *J. Fluid Mech.* **389**, 335–359.
- KIM, K. C. & ADRIAN, R. J. 1999 Very large-scale motion in the outer layer. *Phys. Fluids* **11** (2), 417–422.
- KIM, J. & LIM, J. 2000 A linear process in wall-bounded turbulent shear flows. *Phys. Fluids* **12** (8), 1885–1888.
- KLINE, S. J., REYNOLDS, W. C., SCHRAUB, F. A. & RUNSTADLER, P. W. 1967 The structure of turbulent boundary layers. *J. Fluid Mech.* **30** (04), 741–773.
- LANDAHL, M. T. 1980 A note on an algebraic instability of inviscid parallel shear flows. *J. Fluid Mech.* **98**, 243–251.
- LUCHINI, P. 2000 Reynolds-number-independent instability of the boundary layer over a flat surface: optimal perturbations. *J. Fluid Mech.* **404**, 289–309.
- LUCHINI, P. & BOTTARO, A. 2014 Adjoint equations in stability analysis. *Annu. Rev. Fluid Mech.* **46** (1), 493–517.

- MARQUET, O., LOMBARDI, M. & CHOMAZ, J. M. 2009 Direct and adjoint global modes of a recirculation bubble: lift-up and convective non-normalities. *J. Fluid Mech.* **622**, 1–21.
- MARUSIC, I., MATHIS, R. & HUTCHINS, N. 2010 High Reynolds number effects in wall turbulence. *Intl J. Heat Fluid Flow* **31** (3), 418–428.
- MATHIS, R., HUTCHINS, N. & MARUSIC, I. 2009 Large-scale amplitude modulation of the small-scale structures in turbulent boundary layers. *J. Fluid Mech.* **628**, 311–337.
- MATSUBARA, M. & ALFREDSSON, P. H. 2001 Disturbance growth in boundary layers subjected to free-stream turbulence. *J. Fluid Mech.* **430**, 149–168.
- MCKEON, B. J. & SHARMA, A. S. 2010 A critical-layer framework for turbulent pipe flow. *J. Fluid Mech.* **658**, 336–382.
- MCKEON, B. J., SHARMA, A. S. & JACOBI, I. 2013 Experimental manipulation of wall turbulence: a systems approach. *Phys. Fluids* **25** (3), 031301.
- MOARREF, R., SHARMA, A., TROPP, J. & MCKEON, B. 2013 Model-based scaling of the streamwise energy density in high-Reynolds number turbulent channels. *J. Fluid Mech.* **734**, 275–316.
- MONKEWITZ, P., CHAUHAN, K. & NAGIB, H. 2007 Self-consistent high-Reynolds-number asymptotics for zero-pressure-gradient turbulent boundary layers. *Phys. Fluids* **19** (11), 115101.
- MONTY, J. P., HUTCHINS, N., NG, H. C. H., MARUSIC, I. & CHONG, M. S. 2009 A comparison of turbulent pipe, channel and boundary layer flows. *J. Fluid Mech.* **632**, 431–442.
- ÖSTERLUND, J. M. 1999 Experimental studies of zero pressure-gradient turbulent boundary layer flow. PhD thesis, Royal Institute of Technology (KTH), Stockholm, Sweden.
- PANTON, R. L. 2001 Overview of the self-sustaining mechanisms of wall turbulence. *Prog. Aerosp. Sci.* **37** (4), 341–383.
- PUJALS, G., DEPARDON, S. & COSSU, C. 2010 Drag reduction of a 3D bluff body using coherent streamwise streaks. *Exp. Fluids* **49** (5), 1085–1094.
- REDDY, S. C. & HENNINGSON, D. S. 1993 Energy growth in viscous channel flows. *J. Fluid Mech.* **252**, 209–238.
- REYNOLDS, W. C. & HUSSAIN, A. K. M. F. 1972 The mechanics of an organized wave in turbulent shear flow. Part 3. Theoretical models and comparisons with experiments. *J. Fluid Mech.* **54**, 263–288.
- REYNOLDS, W. C. & TIEDERMAN, W. G. 1967 Stability of turbulent channel flow, with application to Malkus's theory. *J. Fluid Mech.* **27**, 253–272.
- ROBINSON, S. K. 1991 Coherent motions in the turbulent boundary layer. *Annu. Rev. Fluid Mech.* **23** (1), 601–639.
- SCHMID, P. J. & HENNINGSON, D. S. 2001 *Stability and Transition in Shear Flows*. Springer.
- SHARMA, A. S. & MCKEON, B. J. 2013 On coherent structure in wall turbulence. *J. Fluid Mech.* **728**, 196–238.
- SMITS, A. J., MCKEON, B. J. & MARUSIC, I. 2011 High-Reynolds number wall turbulence. *Annu. Rev. Fluid Mech.* **43** (1), 353–375.
- SREENIVASAN, K. R. 1989 The turbulent boundary layer. In *Frontiers in Experimental Fluid Mechanics*, pp. 159–209. Springer.
- TEMPELMANN, D., HANIFI, A. & HENNINGSON, D. 2010 Spatial optimal growth in three-dimensional boundary layers. *J. Fluid Mech.* **646**, 5–33.
- THEODORSEN, T. 1952 Mechanism of turbulence. In *Proceedings of the Second Midwestern Conference on Fluid Mechanics*, pp. 1–18. Ohio State University.
- TOMKINS, C. D. & ADRIAN, R. J. 2003 Spanwise structure and scale growth in turbulent boundary layers. *J. Fluid Mech.* **490**, 37–74.
- TOMKINS, C. D. & ADRIAN, R. J. 2005 Energetic spanwise modes in the logarithmic layer of a turbulent boundary layer. *J. Fluid Mech.* **545**, 141–162.
- UZUN, A., DAVIS, T. B., ALVI, F. S. & HUSSAINI, M. Y. 2017 Optimally growing boundary layer disturbances in a convergent nozzle preceded by a circular pipe. *Theor. Comput. Fluid Dyn.* **770** (1), 124–132.
- VALLIKIVI, M., GANAPATHISUBRAMANI, B. & SMITS, A. J. 2015 Spectral scaling in boundary layers and pipes at very high Reynolds numbers. *J. Fluid Mech.* **771**, 303–326.

- VIOLA, F., IUNGO, G. V., CAMARRI, S., PORT-AGEL, F. & GALLAIRE, F. 2014 Prediction of the hub vortex instability in a wind turbine wake: stability analysis with eddy-viscosity models calibrated on wind tunnel data. *J. Fluid Mech.* **750**, R1.
- WU, X. & MOIN, P. 2009 Direct numerical simulation of turbulence in a nominally zero-pressure-gradient flat-plate boundary layer. *J. Fluid Mech.* **630**, 5–41.